PUCRS

ESCOLA POLITÉCNICA
PROGRAMA DE PÓS-GRADUAÇÃO EM ENGENHARIA E TECNOLOGIA DE MATERIAIS
MESTRADO EM ENGENHARIA E TECNOLOGIA DE MATERIAIS

RAFAEL DIOGO WEIMER

EVALUATION OF CYTOTOXICITY AND REACTIVE OXYGEN SPECIES INDUCED BY GOLD NANOPARTICLES AND 6 MV X-RAYS IN HUMAN GLIOBLASTOMA CELLS

Porto Alegre
2023

PÓS-GRADUAÇÃO - *STRICTO SENSU*

Pontifícia Universidade Católica
do Rio Grande do Sul

ESCOLA POLITÉCNICA
PUCRS
Pontifícia Universidade Católica do Rio Grande do Sul
Programa de Pós-Graduação em Engenharia e Tecnologia de Materiais

EVALUATION OF CYTOTOXICITY AND REACTIVE OXYGEN SPECIES INDUCED BY GOLD NANOPARTICLES AND 6 MV X-RAYS IN HUMAN GLIOBLASTOMA CELLS

RAFAEL DIOGO WEIMER

BACHELOR'S IN MECHANICAL ENGINEERING

DISSERTATION TO OBTAIN THE TITLE OF MASTER IN MATERIALS ENGINEERING AND TECHNOLOGY

Porto Alegre

March, 2023

Pontifícia Universidade Católica do Rio Grande do Sul
ESCOLA POLITÉCNICA
PROGRAMA DE PÓS-GRADUAÇÃO EM ENGENHARIA E TECNOLOGIA DE MATERIAIS

EVALUATION OF CYTOTOXICITY AND REACTIVE OXYGEN SPECIES INDUCED BY GOLD NANOPARTICLES AND 6 MV X-RAYS IN HUMAN GLIOBLASTOMA CELLS

RAFAEL DIOGO WEIMER
BACHELOR'S IN MECHANICAL ENGINEERING

SUPERVISOR: PROF. DR. RICARDO MEURER PAPALÉO

Master's dissertation developed at the Graduate Program in Materials Engineering and Technology (PGETEMA) at the Pontifical Catholic University of Rio Grande do Sul, as part of the requirements for obtaining the title of Master in Materials Engineering and Technology.

Porto Alegre

March, 2023

Ficha Catalográfica

W422e Weimer, Rafael Diogo

Evaluation of cytotoxicity and reactive oxygen species induced by gold nanoparticles and 6 MV X-rays in human glioblastoma cells / Rafael Diogo Weimer. – 2023.

72.

Dissertação (Mestrado) – Programa de Pós-Graduação em Engenharia e Tecnologia de Materiais, PUCRS.

Orientador: Prof. Dr. Ricardo Meurer Papaléo.

1. Gold nanoparticles. 2. ROS. 3. Glioblastoma. I. Papaléo, Ricardo Meurer. II. Título.

Elaborada pelo Sistema de Geração Automática de Ficha Catalográfica da PUCRS com os dados fornecidos pelo(a) autor(a).

Bibliotecária responsável: Clarissa Jesinska Selbach CRB-10/2051

Pontifícia Universidade Católica do Rio Grande do Sul
ESCOLA POLITÉCNICA
PROGRAMA DE PÓS-GRADUAÇÃO EM ENGENHARIA E TECNOLOGIA DE MATERIAIS

EVALUATION OF CYTOTOXICITY AND REACTIVE OXYGEN SPECIES INDUCED BY GOLD NANOPARTICLES AND 6 MV X-RAYS IN HUMAN GLIOBLASTOMA CELLS

CANDIDATO: RAFAEL DIOGO WEIMER

Esta Dissertação de Mestrado foi julgada para obtenção do título de MESTRE EM ENGENHARIA E TECNOLOGIA DE MATERIAIS e aprovada em sua forma final pelo Programa de Pós-Graduação em Engenharia e Tecnologia de Materiais da Pontifícia Universidade Católica do Rio Grandedo Sul.

DR. RICARDO MEURER PAPALÉO - ORIENTADOR

BANCA EXAMINADORA

DR. JARBAS RODRIGUES DE OLIVEIRA - PROGRAMA DE PÓS-GRADUAÇÃO EM BIOLOGIA CELULAR E MOLECULAR - PUCRS

DRA. ROSANE ANGÉLICA LIGABUE - DO PGETEMA - PUCRS

PUCRS
Campus Central
Av. Ipiranga, 6681 - Prédio 32 - Sala 507 - CEP: 90619-900
Telefone: (51) 3353.4059 - Fax: (51) 3320.3625
E-mail: engenharia.pg.materiais@pucrs.br
www.pucrs.br/politecnica

Em algum lugar, algo incrível está esperando para ser descoberto. (Carl Sagan)

DEDICATORY

I dedicated this work to my Family, especially to my mother, Marli Weimer, and to my father, Edison Orli Weimer, who always supported, inspired, and encouraged me to pursue my goals.

ACKNOWLEDGEMENTS

I would like to express my gratitude to Prof. Dr. Ricardo Meurer Papaléo for accepting me into the NANOPUC group, for his guidance, and for giving me the opportunity to carry out this work.

My sincere thanks to Dr. Fernanda Morrone, and the entire Laboratory of Applied Pharmacology for the opportunity of letting me learn and work with cell culture.

To my “personal professor” and friend, Fernando, for his invaluable teachings and support throughout this journey, helping me grow as a person and as a researcher.

To my colleagues at NANOPUC, who helped me learn everything related to nanomaterials and synthesize my first gold nanoparticles.

To the radiotherapy team at Hospital São Lucas da PUCRS, for their assistance with the irradiation experiments.

To all my friends, especially Camila, Ketlin, Augusto, and Elison, for all their advices and for all the great moments we shared.

To all technical staff at PUCRS, for their support with my experiments.

Finally, I am grateful to everyone who, in some way, contributed to making this work possible.

SUMARY

FIGURES

TABLES

SYMBOLS

Ag	Silver
Au	Gold
AuNCs	Gold Nanocomposites
BiO	Bismuth Oxide
CNS	Central Nervous System
Cs-ZnO	Chitosan zinc oxide
DCFH-DA	2′,7′-Dichlorofluorescin diacetate
Dh	Mean hydrodynamic diameter averaged by number
DNA	Deoxyribonucleic acid
GBM	Glioblastoma multiforme
GdNP	Gadolinium Nanoparticle
GNP	Gold Nanoparticles
GNP@DX	Dextran coated gold nanoparticles
HAuCl4	Chloroauric acid
IR	Ionizing Radiation
LET	Linear Energy Transfer
MeV	Mega electron volt
MV	Mega Volt
NaBH4	Sodium Borohydride
NPs	Nanoparticles
PDI	Polydispersity index
PBA	Poly butylene Adipate
PBS	Phosphate Buffer Saline
PEG	Polyethylene Glycol
Pt	Platinum
ROS	Reactive Oxygen Species
RT	Radiotherapy
SPIONS	Superparamagnetic iron oxide nanoparticles
TEM	Transmission electron microscopy
WHO	World Health Organization
Z	Atomic Number

RESUMO

WEIMER, Rafael Diogo. **Avaliação da citotoxicidade e das espécies reativas de oxigênio induzidas por nanopartículas de ouro e raio-X de 6 MV em células de glioblastoma humano.** Porto Alegre. 2023. Dissertação. Programa de Pós-Graduação em Engenharia e Tecnologia de Materiais, PONTIFÍCIA UNIVERSIDADE CATÓLICA DO RIO GRANDE DO SUL.

O câncer é um problema de saúde pública e uma das principais causas de morte ao redor do mundo. Inúmeros estudos estão sendo desenvolvidos para melhorar os efeitos da radioterapia, focando no desenvolvimento de radiosensibilizadores. Nanopartículas (NPs) de ouro apresentam diversas aplicações biomédicas, incluído a possibilidade de serem utilizadas como radiosensibilizadores no tratamento de câncer. Nesse contexto, o objetivo deste trabalho foi investigar os efeitos de nanopartículas de ouro sem recobrimento (GNP) e recobertas com dextrana aminada (GNP@DX-NH_2) em combinação ou não com irradiação de raio-X de um equipamento clínico de 6 MV, em células de glioblastoma humano (U87). Foram sintetizadas GNP e GNP@DX-NH_2 com núcleo metálico de 11,9 nm e 8,0 nm, respectivamente. Ensaios de toxicidade demonstraram que as NPs não são tóxicas em concentrações de até 50 µg/mL. A avaliação da internalização das NPs por microscopia de transmissão indica que as elas se distribuem de forma heterogênea no citoplasma, a maior parte agregada dentro de vesículas ou soltas no citoplasma. A avaliação das espécies reativas de oxigênio (EROs) após o tratamento com NPs por 24h indica um aumento de 38% e 54% para as GNP e GNP@DX-NH_2, respectivamente. Quando combinadas com irradiações de 2 Gy e 6 Gy, os grupos tratados com GNP tiveram um aumento aproximado de 70% em relação ao grupo controle não irradiado para as duas doses de radiação, enquanto os grupos tratados com GNP@DX-NH_2 induziram um aumento de 60% para 2 Gy e 88% para 6 Gy. Os resultados demonstram que esse efeito pode ser em parte associado a produção de EROs devido a presença das NPs sem irradiação, e apenas levemente aumentado quando houve a combinação de NPs e irradiação.

Palavras-Chaves: Nanopartículas de ouro, ROS, glioblastoma.

ABSTRACT

WEIMER, Rafael Diogo. **Evaluation of cytotoxicity and reactive oxygen species induced by gold nanoparticles and 6 MV X-Rays in human glioblastoma cells.** Porto Alegre. 2023. Master Thesis. Graduation Program in Materials Engineering and Technology, PONTIFICAL CATHOLIC UNIVERSITY OF RIO GRANDE DO SUL.

Cancer is a public health problem and one of the main causes of death around the world. Numerous studies are being carried out to improve the effects of radiotherapy, focusing on the development of radiosensitizers. Gold nanoparticles (NPs) have several biomedical applications, including the possibility of being used as radiosensitizers for cancer treatment. In this context, the aim of this work was to investigate the potential effects of gold nanoparticles without coating (GNP) and aminated dextran-coated gold nanoparticles (GNP@DX-NH_2) in combination or not with X-ray irradiations from a 6 MV clinical equipment, in human glioblastoma cells (U87). GNP and GNP@DX-NH_2 with metallic core of 11.9 nm and 8.0 nm, respectively, were synthesized. Toxicity assays demonstrated that NPs are not toxic at concentrations up to 50 µg/mL. The evaluation of the internalization of NPs by transmission microscopy indicated that they were heterogeneously distributed in the cytoplasm, mostly aggregated within vesicles or loose in the cytoplasm. The evaluation of reactive oxygen species (ROS) after treatment with NPs for 24h indicated an increase of 38% and 54% for GNP and GNP@DX-NH_2, respectively. When combined with irradiation of 2 Gy and 6 Gy, the groups treated with GNP had an approximated increase of 70% in ROS levels relative to the non-irradiated control for both radiation doses, while the groups treated with GNP@DX-NH_2 induced an increase of 60% for 2 Gy and 88% for 6 Gy. The results demonstrate that this effect could be associated with the production of ROS induced mostly by the NPs before the irradiations, and only slightly increased after the combination of NPs and radiation treatment.

Keywords: Gold nanoparticles, ROS, glioblastoma.

1. INTRODUCTION

Cancer is a public health problem and it is one of the main causes of death around the world. According to the World Health Organization (WHO), it caused almost 10 million deaths in 2020 [1], and this number is expected to be 12.9 million in 2030 [2], a rise of 29.9% compared to 2020. Among the several types of cancers, the Central Nervous System (CNS) malignant tumors in the brain and spinal cord represent 2.5% of cancer deaths [2]. Of the malignant primary tumor types of the CNS, Glioblastoma (GBM) is one of the most common and deadly [3 - 5]. In a scale from I to IV, elaborated by the WHO, GBM is classified as a grade IV glioma, due to its aggressive and invasive characteristics [6, 7]. Despite the low incidence rate, GBM is a clinical problem due to its poor prognosis. The tumor spreads aggressively through the brain's health tissue, leading to different neurological damages, and even with the proper treatment, the chance of recurrence is high [5, 6, 8].

The primary treatment of GBM encompasses surgical removal of the maximum tumor volume, followed by radiotherapy (RT) associated with temozolomide chemotherapy [3, 4, 6, 9]. Due to its infiltrative characteristic, not all cancer cells can be reached and removed by surgery, so RT is an important post-operatory tool. For GBM, a complete radiotherapy treatment is divided into a small series of daily doses of 2 Gy during 30 sessions, for a total dose of 60 Gy [3 – 6]. Given the aggressive nature of GBM, the development of new treatments and strategies to enhance the effects of radiotherapy and improve patient outcomes is essential, not only for glioblastoma but for all types of cancer. One promising approach is the use of radiosensitizers: compounds that, when combined with RT, can enhance its tumor-killing effects [10].

The potential use of metallic nanoparticles as radiosensitizers has drawn significant attention from researchers in recent years. Numerous studies have evaluated their effects on the treatment of different types of cancer [11-14]. Among them, gold nanoparticles (GNPs) are one of the most extensively studied. There are several reasons for that. GNPs are biocompatible and possess a high atomic number (Z = 79), which increases the probability of interaction of GNPs with high-energy photons, leading to an increase in the energy deposition inside the tumor region. Furthermore, GNPs can be coated with different molecules, such as proteins and polymers, that can influence how NPs interact with cells, as well as the cellular response to the radiation treatment.

Despite the large number of works on NPs as cancer radiosensitizers, there are still many open questions on the mechanism underlying the radiosensitization effect promoted by them. Initially, it was believed that the increased energy deposition in the tumor microenvironment caused by the NP's presence was responsible for the radiosensitization effect. But theoretically, this physical effect is only effective for keV X-rays, and it is not expected to play a major role in MeV treatments. However, contrary to theory and simulation results, different *in vitro* and *in vivo* studies show that NPs induce radiosensitization effects for X-ray energies up to MeV [15]. Therefore, it is clear that there are other biological and chemical mechanisms involved in the radiosensitization promoted by NPs, which must be investigated. One of these mechanisms is the enhanced generation of reactive oxygen species (ROS), free radicals produced by water radiolysis during radiotherapy, which can cause irreversible damage to DNA and other cellular organelles [16, 17].

In this work, uncoated and dextran-coated GNPs were synthesized, and the cytotoxicity, the effect of the coating on the cellular uptake, and the generation of reactive oxygen species induced by the presence of GNPs in human glioblastoma cells irradiated with 6 MV X-rays were investigated. The irradiations were performed in a 6 MV clinical accelerator at the Radiotherapy Center of Hospital São Lucas and the *in vitro* studies were performed at the Applied Pharmacology Laboratory of PUCRS.

2. OBJECTIVES

The main goal of this study is to synthesize uncoated and dextran-coated gold nanoparticles and investigate their effects in human glioblastoma cells exposed to 6 MV photon beams from a clinical linear accelerator.

2.1. Specific Objectives

- Synthesize and characterize uncoated and dextran-coated gold nanoparticles;
- Investigate the cytotoxicity of gold nanoparticles in U87 and M059J glioblastoma cells treated with different nanoparticle concentrations;
- Evaluate the influence of the dextran coating on the cellular uptake of NPs;
- Quantify the generation of Reactive Oxygen Species (ROS) induced by the presence of NPs in glioblastoma cells treated with two different radiation doses.

3. BASIC PRINCIPLES

3.1. Principles of radiobiology

Radiobiology studies the interaction of ionizing radiation (IR) with biological matter and its potential effects. IR is used in radiotherapy to treat malignant tumors by exposing them to a source of radiation with enough energy to induce ionization damage in cancer cells [5]. There are different types of IR, including X-rays, gamma rays, and high-energy charged particles, such as electrons, ions, and neutrons [9]. According to the American Cancer Society [18], external beam radiation therapy (EBRT) using photons is the most common type of radiation therapy utilized to treat cancer.

3.1.1. Interaction of photons with matter

Photons are uncharged particles that interact with matter by colliding with orbital electrons or directly with the atomic nuclei. In these interactions, the incident photon can lose a fraction or all of its energy, which is transferred to the electrons by three different processes: the photoelectric effect, the Compton effect, and pair production [5, 19, 20].

In the photoelectric effect, an electron, usually from the K level, completely absorbs a photon and is ejected from the atom with a specific kinetic energy (Figure 3.1a). This process leads to a cascade of events, where an electron from an outer level occupies the K level vacancy, and the excess of energy is emitted in the form of photons (called characteristic X-ray) or transmitted to an orbital electron, which is also ejected from the atom (called Auger electron) [5, 19, 20]. If the ejected electrons have enough energy, they can interact with other atoms and generate further excitation or ionization [21].

In the Compton effect, an electron from an outer orbital of the atom interacts with a photon and absorbs part of its energy, being ejected [9] (Figure 3.1b). In this interaction, the incident photon is scattered and loses part of its energy, but still can interact with other electrons. Pair production can occur when photons with energy greater than 1,022 MeV interact with the nuclear field, generating an electron-positron pair (Figure 3.1c) [5]. The generated electron can interact with other atoms, while the positron is rapidly annihilated by a free electron, generating two characteristic photons of 0,511 MeV [9].

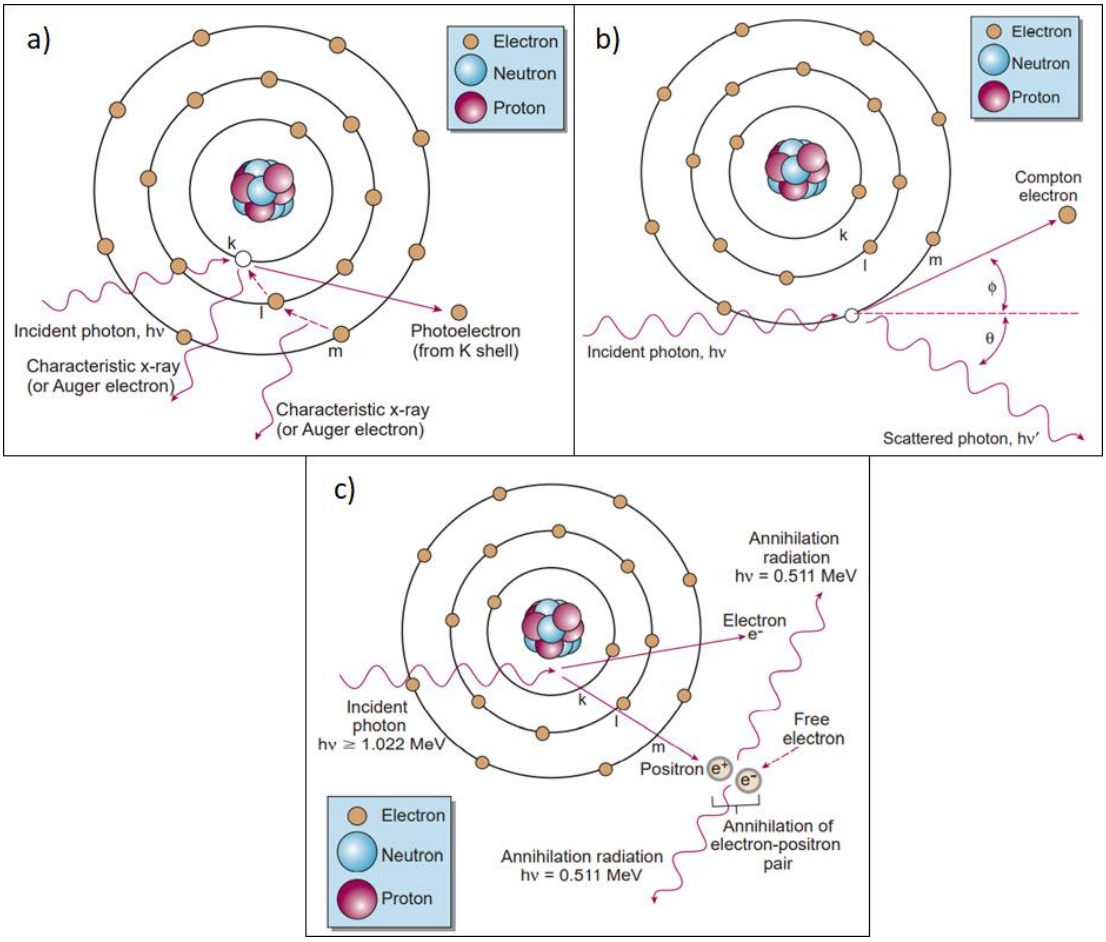

Figure 3.1. Representation of the main mechanisms of energy transfer from photons to electrons. a) photoelectric effect. b) Compton effect. c) Pair production. Adapted from [9].

Figure 3.2 illustrates the relative importance of each interaction mechanism in matter ionization, depending on the photon energy and the atomic number of the material. Considering that biological tissue, which is primarily composed of water, has an atomic number (Z) of around 7.4, the Compton effect is the predominant

mechanism of interaction at clinical photon energies [5]. The photoelectric effect becomes more significant for high-Z materials and at lower photon energies, but decreases as photon energy increases. Its probability of occurrence depends on the atomic number of the material being irradiated and is proportional to Z^3. Pair production is only relevant at very high photon energies and high-Z materials [19, 20, 22] and can usually be neglected for clinical beams.

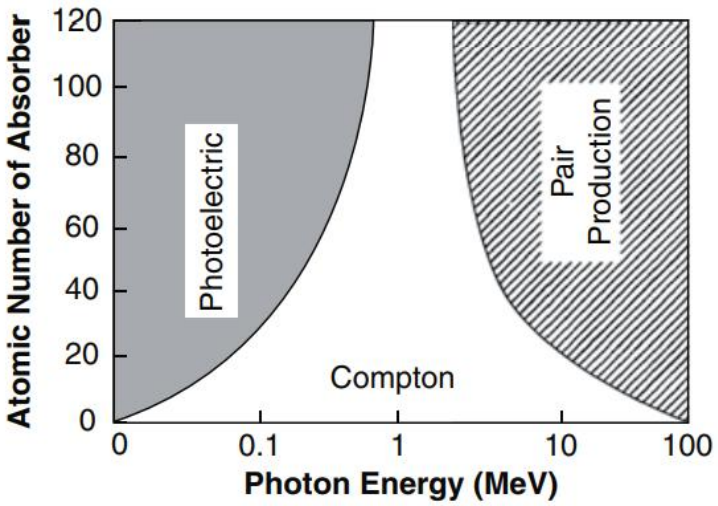

Figure 3.2. Contribution of different interaction mechanisms to matter ionization as a function of atomic number and photon energy. Adapted from [19].

The term Linear Energy Transfer (LET) is used to express the quantity of energy deposited by a particle of ionizing radiation per unity length as it crosses the biological tissue [5, 23]. Photons and electron beams are classified as low-LET radiation because they generate low ionization densities in matter, meaning they interact sparsely with the atoms along their path as they cross the material. Neutrons, alpha particles, and heavy ions, on the other hand, are called high-LET radiation, as they interact more strongly with matter [9, 24], inducing high levels of ionization density along their path. Figure 3.3 shows the difference in the ionization density for different types of ionizing particles.

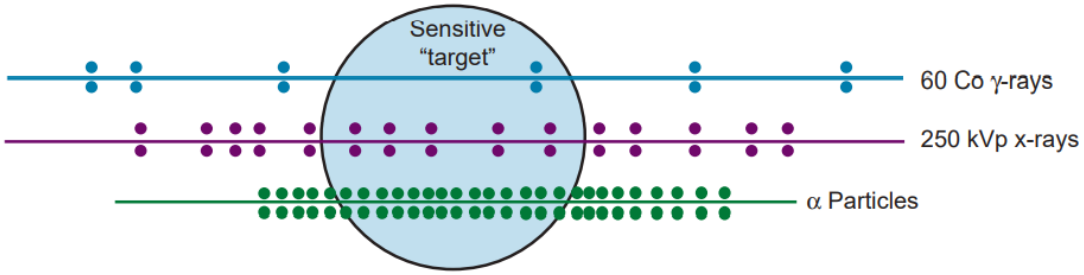

Figure 3.3. Representation of the density of ionization events for particles with different LET. The dots along the tracks represent ionization events in the biological tissue. High-LET ionizing radiation, such as alpha particles, results in more closely spaced ionization events, leading to more energy deposition in the target volume. Adapted from [9].

3.1.2. Radiation effects at the cellular level

DNA is the most critical target in radiotherapy treatment [19, 21]. Since each cell contains only a single DNA molecule, radiation-induced damage can lead to cellular death, depending on the intensity and the cellular repair response. DNA damage is classified as direct or indirect. When DNA is damaged directly by a photon particle or a secondary electron ejected by an atom, the damage is considered direct [25] (Figure 3.4). This is the main mechanism of action for high-LET radiation [26] and accounts for approximately one-third of all biological damage caused by low-LET radiation [21].

In contrast, indirect damage occurs when free radicals, produced through the interaction of ionizing radiation with other cellular molecules, damage the DNA (Figure 3.4) [26]. The indirect effect occurs predominantly with low-LET photons and accounts for nearly two-thirds of all its biological damage [21]. Given that the cellular environment is composed of approximately 70% – 80% water [26, 27], free radicals are mainly produced by the interaction of radiation with water molecules, leading to water radiolysis.

During water radiolysis, water molecules can undergo either ionization or excitation. In the ionization process, a water molecule (H_2O) loses an electron (e^-), forming H_2O^+. The H_2O^+ ion rapidly decomposes into H^+ and a hydroxyl radical ($\cdot OH$), while the emitted electron (e^-) can interact with other water molecules, becoming a hydrated electron (e^-_{aq}). In the excitation process, the excited water

molecule (H_2O^*) decomposes into a hydrogen radical (H·) and a hydroxyl radical (·OH). The free radicals produced through both processes can further react with each other and with other molecules, resulting in various byproducts. After this extremely fast process, different types of reactive oxygen species (ROS) are produced, including ·OH, O_2^{-}·, and H_2O· [26 - 29]. They are highly reactive due to their unstable chemical nature, and when they interact with cellular organelles, such as DNA strands, biological damage occurs [26, 27, 29].

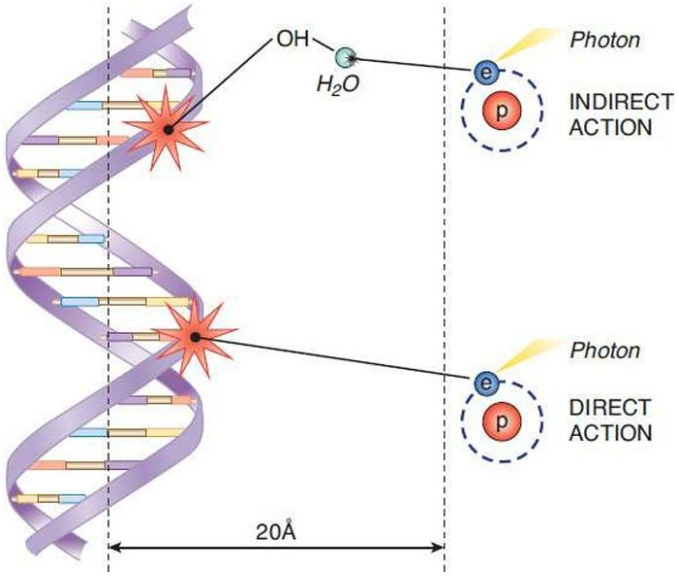

Figure 3.4. Representation of DNA damage by direct and indirect action. Adapted from [25].

The entire process of radiation interaction can be divided into three distinct phases. The first phase, known as the physical phase, involves the deposition of energy by the radiation beam within the cellular environment. Primary excitations and ionizations result in a cascade of secondary electrons that distribute the initial deposited energy across larger volumes inside the cell. This phase is extremely short, lasting approximately 10^{-15} s [30].

Following the physical phase comes the chemical phase, which involves the generation of free radicals, such as ROS. These highly reactive species can damage various molecules, including DNA, proteins, and other cellular organelles. The entire chemical process takes place around 10^{-6} s after exposure to radiation [28]. Finally, the biological phase corresponds to the period during which cells attempt to repair the damage induced by radiation or caused by free radicals. This process can take

from 10^{-3} s to several days or weeks, potentially leading to cell death or mutations, if DNA damage is not properly repaired [9, 28, 30].

3.2. Gold nanoparticles in biomedicine

In the last decades, there has been a growing research interest in nanomaterials due to their unique properties and wide range of applications, from environment remediation [31, 32] to energy production [33, 34] or biomedicine [11-14].

In the biomedical field, gold nanoparticles are one of the most studied nanoparticles, known for their biocompatibility, low cytotoxicity, and tunable physicochemical properties. By controlling the synthesis parameters (e.g., time, pH, temperature, and reagent concentrations), GNPs can be engineered to have different sizes and shapes, like spheres, stars, or rods (Figure 3.5) [35 – 37]. Furthermore, their surface properties can be modified by coating them with different substances, such as polymers and proteins, or by conjugating them with drugs, peptides, antibodies, and other small molecules.

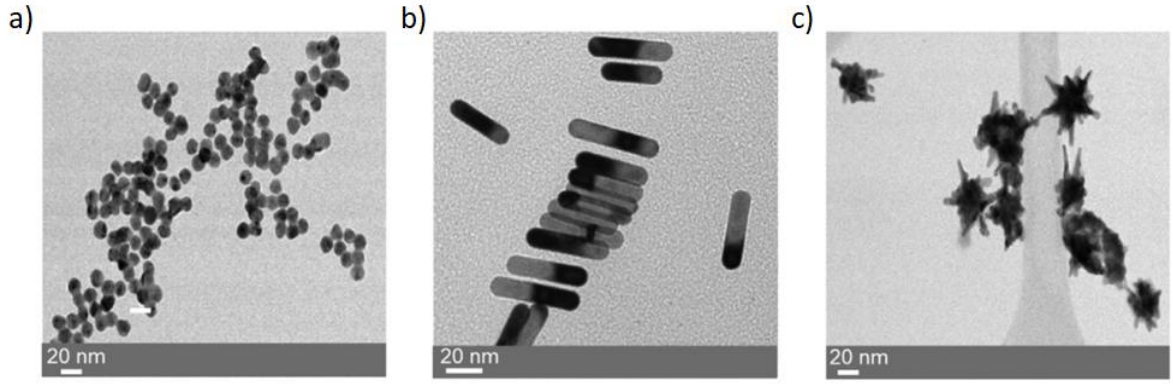

Figure 3.5. Examples of GNPs with different morphologies. Transmission Electron Microscopy of gold a) nanospheres, b) nanorods, c) nanostars. Adapted from [35].

One of the applications of GNPs in the biomedical field is as imaging probes. They are good candidates for contrast agents in computed tomography (CT) due to their high atomic number and large X-ray attenuation coefficient [38]. Additionally, GNPs can be conjugated with radionuclides and used as radioisotope carriers for

Positron Emission Tomography (PET) and Single Photon Emission Computed Tomography (SPECT) [39, 40]. Studies also highlight their potential as probes in photoacoustic imaging due to their high photothermal conversion efficiency [41, 42]. Moreover, the possibility of conjugation and surface modification of GNPs with different molecules make them promising candidates as drug delivery systems in cancer treatment [43]. Another important application, described below, is their use to enhance radiotherapy treatment, the main topic of this study.

3.2.1. Gold nanoparticles as radiosensitizers

One strategy to enhance the effects of radiotherapy is to use molecules or drugs known as radiosensitizers, which increase the cell-killing effects of radiation. Metallic nanoparticles are among the potential candidates, and numerous studies have demonstrated their excellent potential. Table 3.1 summarizes a few examples from the literature.

Table 3.1. Summary of *in vitro* studies investigating metallic nanoparticles as radiosensitizers.

Nanoparticle	Conjugation	Size	Cell line	Radiation source	Year	Ref.
PEG coated Ag@Au core-shell	GMT8 aptamer	11 nm	U87	6 MV X-rays	2022	[44]
Dx Coated SPIONs **GNPs**	-	5.9 nm 5.2 nm	U87 M059J	6 MV X-rays	2022	[45]
PEG-PBA-PEG coated SPIONS	Folic acid Temozolomide	17 nm	C6	6 MV X-rays	2022	[46]
BiO	-	80 nm	MCF-7	6 MV X-rays	2022	[47]
GNPs	-	15 nm	MDA-MB-231	6 MV X-rays 100 kV X-rays 190 kV X-rays	2022	[48]
Pt	-	3.2 nm	MDA-MB-231 T47D	137Cs	2021	[49]
ZnO **Cs-ZnO biocomposite**	-	50 nm 30 nm	MDA-MB-231	6 MV X-rays	2021	[50]
GaNPs **AuNPs** **SPIONs**	-	1.9 nm 3 nm 140 nm	U87 MCF-7	6 MV X-rays	2020	[51]
BSA-AuNCs	Folic acid Trastuzumab	10 nm	SK-BR3 L929	6 MV X-rays	2020	[52]

Table 3.1. Summary of *in vitro* studies investigating metallic nanoparticles as radiosensitizers.

Nanoparticle	Conjugation	Size	Cell line	Radiation source	Year	Ref.
Gd doped ZnO	-	9 nm	SKLC-6	6 MV X-rays	2019	[53]
GNPs **SPIONs** **Pt** **BiO**	-	1.9 nm 15 nm 42 nm 70 nm	HCT116	150 MeV protons	2019	[54]
SiO2@Au core-shell	-	25 nm	MCF-7	6 MV X-rays 18 MV X-rays	2018	[55]
Cysplatin and Glucose coated GNPs	-	20 nm	A431	6 MV X-rays	2018	[56]

Besides other features, metallic nanoparticles have a higher atomic number than biological tissue, especially gold (Z = 79), bismuth (Z = 83), and platinum (Z = 78), resulting in an increased photon mass energy absorption coefficient (Figure 3.6). Therefore, the presence of GNPs inside tumor cells during irradiation can enhance the physical effects of radiotherapy. When irradiated, GNPs have a higher probability of interacting with photons, mainly through the Compton and photoelectric effects [57]. These interactions lead to the emission of secondary and Auger electrons from the NPs, increasing energy deposition within the tumor microenvironment and potentially causing greater cellular damage. As shown in Figure 3.6, the most significant difference between the mass energy absorption coefficient of gold and soft tissue occurs in the keV energy range. However, Monte Carlo simulations indicate that GNPs also increase secondary electron production at MeV energies [58].

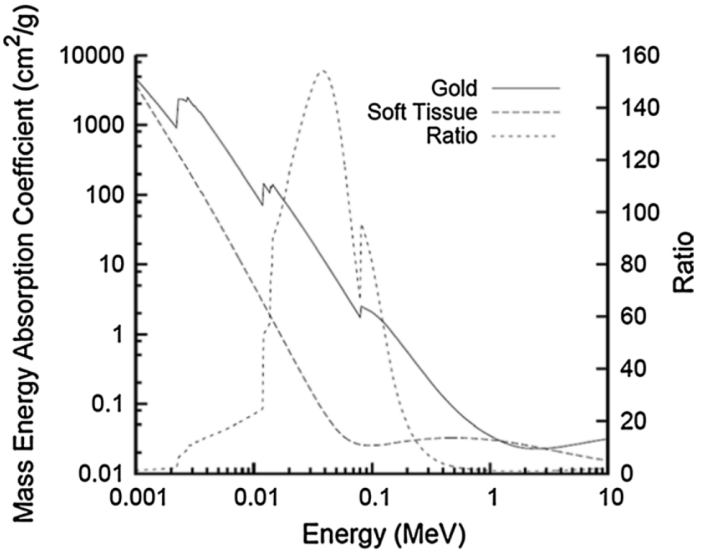

Figure 3.6. Comparison between Gold and Soft Tissue mass energy absorption coefficient as a function of Photon Energy. Adapted from [57].

Furthermore, the presence of nanoparticles within the cytoplasm during the irradiation process may interfere with the chemical environment, increasing the generation of ROS [47, 54, 59, 60, 61]. Studies suggest that the surface of certain NPs can act as a catalyst, reducing the energy required to break the H-OH bonds in surrounding water molecules [62, 63], thus facilitating ROS production. Moreover, electrons ejected from NPs during irradiation can interact with nearby water molecules, increasing water radiolysis and the formation of more free radicals [64], as described in Section 3.1.2. Depending on the intracellular location where these free radicals are produced, they can damage different cellular structures, resulting in DNA damage, lipid membrane peroxidation, disruption of the mitochondrial electron transport chain, or protein misfolding [16, 65, 66]. Figure 3.7 presents a schematic overview of the physical and chemical processes described in this section that occurs during X-ray irradiation of cancer cells in the presence of GNPs.

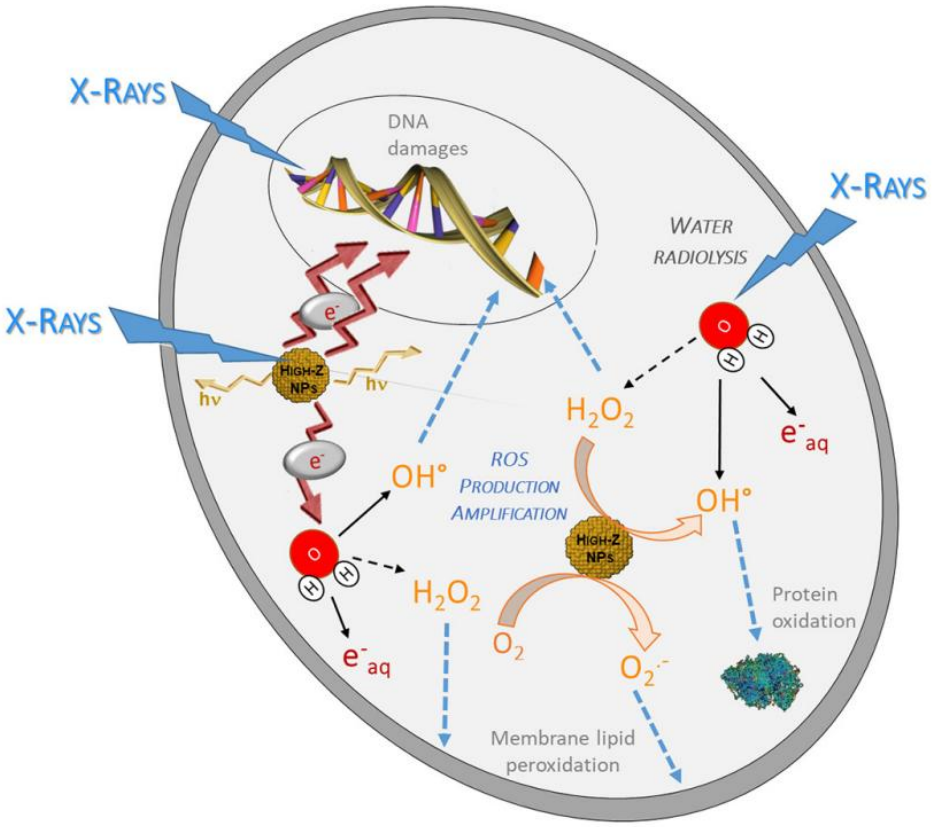

Figure 3.7. Representation of different processes occurring under X-ray irradiation. The interaction of X-rays with cellular molecules results in ionization and excitation, resulting in direct DNA damage or the production of ROS through water radiolysis. ROS can further interact with other cellular components, causing protein oxidation or misfolding, membrane lipid peroxidation, and damage to mitochondria or DNA. The incorporation of gold nanoparticles can increase the physical and chemical effects by generating more secondary electrons and amplifying ROS production. Adapted from [66].

The main effect of radiosensitization induced by NPs is increased DNA damage, either directly through enhanced energy deposition or indirectly via elevated ROS production [67 – 69]. However, in addition to the physical and chemical effects of NPs during radiation treatment, they can also induce biological effects. One of the possible biological effects is the disruption of the cell cycle. The cell cycle is a complex network of mechanisms that regulate cellular division. In cancer cells, this process is dysregulated, leading to uncontrolled growth [70]. Studies have shown that NPs can promote cell cycle arrest at different phases, depending on the cell line and the NPs system, interfering with and controlling tumor growth [71 – 75]. Additionally, NPs can dysregulate the expression levels of different genes and proteins [15, 76], and elevated ROS levels after radiation exposure can activate

apoptotic and necrotic pathways by dysregulating the expression of specific proteins, such as P53 [16, 65, 77].

4. MATERIALS AND METHODS

4.1. Synthesis of nanoparticles

4.1.1. Gold nanoparticles (GNPs)

Naked gold nanoparticles were synthesized following a protocol adapted from Guerra et al. [45]. Briefly, 500 mL of a solution of 0.2 mM $HAuCl_4 \cdot 3H_2O$ (99%, Sigma-Aldrich) were added to a glass reactor with an internal capacity of 1 L. Then, 20 mL of 24.4 mM $NaBH_4$ were added dropwise over approximately fifteen minutes under constant magnetic stirring at room temperature. After the addition of $NaBH_4$, the mixture was stirred for another fifteen minutes. The resulting suspension was concentrated by centrifugation at 4000 rpm for 10 minutes using a centrifugal filter (50 kDa Amicon) and washed twice with Milli-Q water. The final volume of GNPs was resuspended in Milli-Q water and stored at 4°C.

4.1.2. Aminated dextran-coated gold nanoparticles (GNP@DX-NH_2)

Dextran-coated gold nanoparticles (GNP@DX) were prepared *in situ* following a protocol adapted from Jang et al. [78]. First, 12 g of Dextran T-10 (molecular weight ~10 kDa, Pharmacosmos) were dissolved in 160 mL of Milli-Q water in a three-neck round-bottom glass reactor and homogenized for 1 hour under constant magnetic stirring. Then, the mixture was heated to 85°C, and 1.1 mL of 1M NaOH was added to adjust the pH around 10. Next, 2.26 mL of a solution containing 9.6 mg/mL of $HAuCl_4 \cdot 3H_2O$ was added dropwise, causing the mixture to immediately change color from translucid to ruby-red. The mixture was maintained under constant magnetic stirring at 85°C for 30 minutes, then cooled to room temperature. The product was centrifuged using a 50 kDa Amicon filter at 7000 rpm for 15 minutes, then washed four times with Milli-Q water to remove the excess of free dextran.

After the washing steps, the dextran coating was cross-linked (GNP@DX-CL) with epichlorohydrin to chemically bind the dextran molecules, forming a stable network around the gold nanoparticles. The concentrated solution of GNP@DX from the previous step was diluted to a final volume of 4 mL. Then, 200 µL of a 1M NaOH solution was added, followed by 100 µL of epichlorohydrin (Sigma-Aldrich). The solution was stirred for approximately 14 h at room temperature, then centrifugated with 50 kDa Amicons (10 min at 7000 rpm) and washed three times with Milli-Q water.

The final step was the amination of the dextran surface coating (GNP@DX-NH_2). The GNP@DX-CL were resuspended to a final volume of 4 mL, followed by the addition of 2.1 mL of 28% NH_4OH. The solution was left to react for 24 h under constant magnetic stirring at room temperature, then concentrated with 50 kDa Amicons (5000 rpm for 5 minutes) and washed with Milli-Q water to remove excess NH_4OH. After each washing cycle, the pH of the residual water was measured, and the process was repeated until it reached approximately 7. The concentrated solution was diluted to a final volume of 5 mL and stored at 4°C.

4.2. Characterization of nanoparticles

4.2.1. Dynamic light scattering (DLS) and Zeta potential (ZP)

The mean hydrodynamic diameter and zeta potential of the nanoparticles were measured using a Zetasizer, model ZEN3600 – Malvern. For this, the nanoparticles were dispersed in Milli-Q water to a final volume of 1 mL at a concentration of 0.1 mM and measured at room temperature (25°C).

4.2.2. UV-Vis spectroscopy

The absorption spectra of the nanoparticles were obtained using a Perkin Elmer Lambda 35 spectrophotometer. The nanoparticles were diluted in Milli-Q water to a final concentration of 0.1 mM, and the absorption spectra were measured in the spectral region of 400 to 800 nm.

4.2.3. Transmission electron microscopy (TEM)

Images of nanoparticles were obtained by transmission electron microscopy (TEM) with a Tecnai G2 T20 – FEI microscope at the Central Laboratory of Microscopy and Microanalysis (LabCEMM, PUCRS). A drop of NP solution was placed onto carbon grids and left to dry for 24 h before analysis. The morphology and size distribution of NPs were evaluated from TEM images using *imageJ software,* analyzing at least 100 particles of each NP type.

4.3. *In vitro* assays

The cytotoxicity of GNPs and GNP@DX-NH_2 was evaluated in two human glioblastoma cell lines, M059J and U87-MG, as well as in the Vero cell line, which was used as a healthy tissue control. The intracellular distribution of both NPs and the quantification of ROS levels after irradiation were evaluated in U87 cells.

4.3.1. Cell culture

Cell culture procedures were conducted at the Laboratory of Applied Pharmacology of PUCRS. Vero and U87 cells were cultured with Dubelcco's Modified Eagle's Medium (DMEM), while M059J cells were cultured with Dubelcco's Modified Eagle's Medium Nutrient Mixture F-12 (DMEM/F12). Both media were supplemented with 10% fetal bovine serum (FBS), 1% penicillin, and 0.1% fungizone, and cells were maintained in a humidified incubator at 37°C with 5% CO_2.

4.3.2. Viability assay

The cytotoxicity of nanoparticles was evaluated using the MTT assay, which measures cellular viability based on mitochondrial activity. In viable cells, MTT (3-(4,5-dimethylthiazol-2-yl)-2,5-diphenyl tetrazolium bromide) is internalized and reduced by active mitochondria into insoluble formazan crystals. These crystals are then dissolved in DMSO and quantified by spectrophotometry [79].

U87, M059J, and Vero cells were plated in 96-well plates at a density of 5,000 cells per well. After 24 h, they were treated with different concentrations of NPs (0, 5, 10, 20 e 50 µg/mL) and incubated for additional 24 h. The medium containing the nanoparticles was then discarded, the cells were washed once with PBS, and fresh DMEM containing 10% MTT solution (5 mg/mL) was added. After 3 h of incubation, the medium was discarded, and 100 µL of DMSO was added to each well to solubilize the formazan crystals formed. The absorbance was measured at 490 nm using a Multilabel Plate Reader Platform (Victor X3, model 2030, Perkin Elmer). The mean absorbance value of each treatment was compared to the control, and the results were expressed as the percentage of viability relative to the control.

4.3.3. Evaluation of the intracellular distribution of nanoparticles

The intracellular distribution of NPs was analyzed by TEM. U87 cells were plated in 6-well plates (5 x 10^4 cells/well) and allowed to grow for 24 h. Then, cells were treated with NPs at a concentration of 20 µg/mL for 24 h, washed once with PBS, trypsinized, and centrifuged at 2000 rpm for 5 min. The resulting pellets were fixed with a solution of 2.5% glutaraldehyde, 2% paraformaldehyde, and phosphate buffer, then post-fixed with a 1% Osmium Tetroxide solution in 0.1 M phosphate buffer and dehydrated in acetone at different concentrations (30%, 50%, 70% and 100%). The samples were embedded in epoxy resin, cut by microtomy, and stained with uranyl acetate and lead citrate. Images were acquired in a FEI Tecnai G2 T20 microscope.

4.3.4. X-ray irradiation

The cells were irradiated in a 6 MV linear accelerator (Clinac IX, Varian) located at the Radiotherapy Center of Hospital São Lucas at PUCRS, following a procedure developed and described by Guerra et al. [45]. Briefly, the cell plate was placed inside a 30 cm x 30 cm acrylic sample holder positioned between two solid water bolus plaques. The top plate had a thickness of 5 cm and the bottom plate 3 cm. Figures 4.1a and 4.1c illustrate the setup arrangement for irradiation.

The irradiation planning was done using *Eclipse* software by the medical physics team at São Lucas Hospital. Irradiations were performed at a dose rate of approximately 1 Gy/min, within a 20 X 20 cm field, at a source-to-surface distance (SSD) of 93 cm. This setup ensured that the isodose curves (lines where the same radiation dose is delivered) were uniform in the region of the cell plate (Figure 4.1b). The total doses used were 2 and 6 Gy.

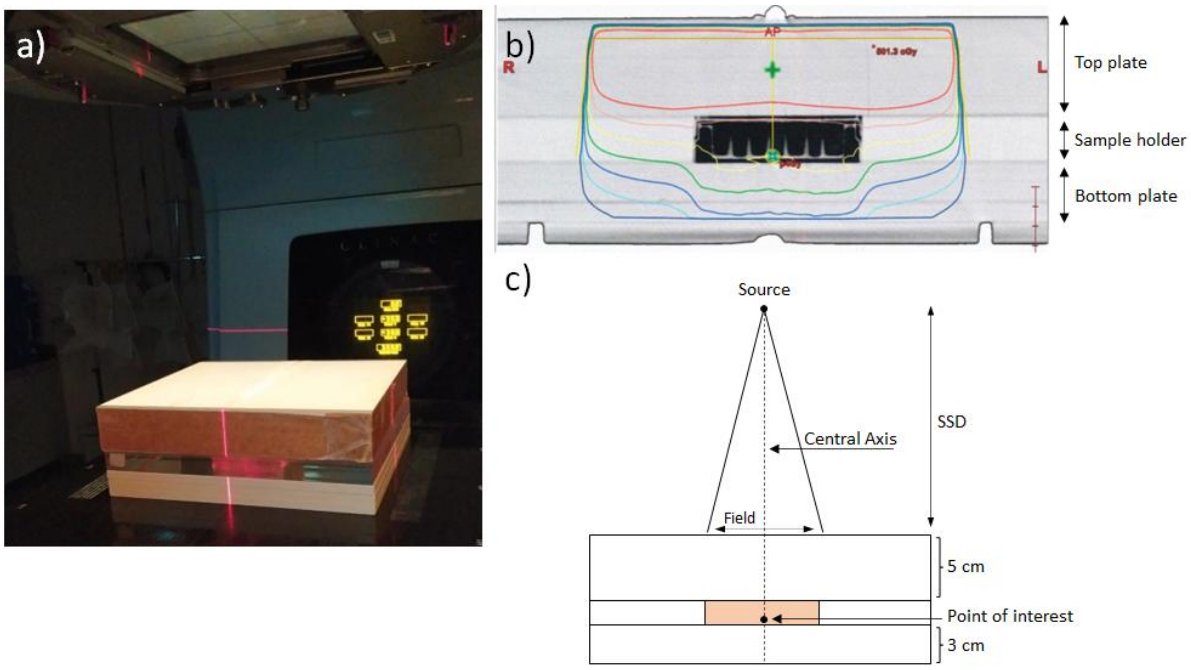

Figure 4.1. a) Irradiation setup. An acrylic sample holder containing the cell plate is positioned between two solid water bolus plaques. b) Transversal tomographic image of the sample holder. The colored lines represent the isodose curves, with the isocenter located at the same position as the cell plate (black region). c) Representation of the irradiation geometry. The point of interest, where the cells are located, coincides with the isodose curve.

4.3.5. Quantification of reactive oxygen species

To quantify intracellular ROS generation in NPs-treated and irradiated cells, the DCFH-DA assay was employed. DCFH-DA (2′,7′-dichlorodihydrofluorescein diacetate) is a non-fluorescent compound that permeates the cells and is deacetylated by intracellular esterases, resulting in the formation of DCFH (2′,7′-dichlorodihydrofluorescein). In the presence of ROS, DCFH is oxidized into DCF (2’-7’dichlorofluorescein), a fluorescent molecule with excitation at 485 nm and emission at 530 nm [80] (Figure 4.2). DCFH-DA is a non-specific probe that reacts with various

ROS and their byproducts, including ·OH, $O_2^{\cdot-}$, H_2O_2, $^1O_2$, and is commonly used as a ROS quantification method [80 - 83].

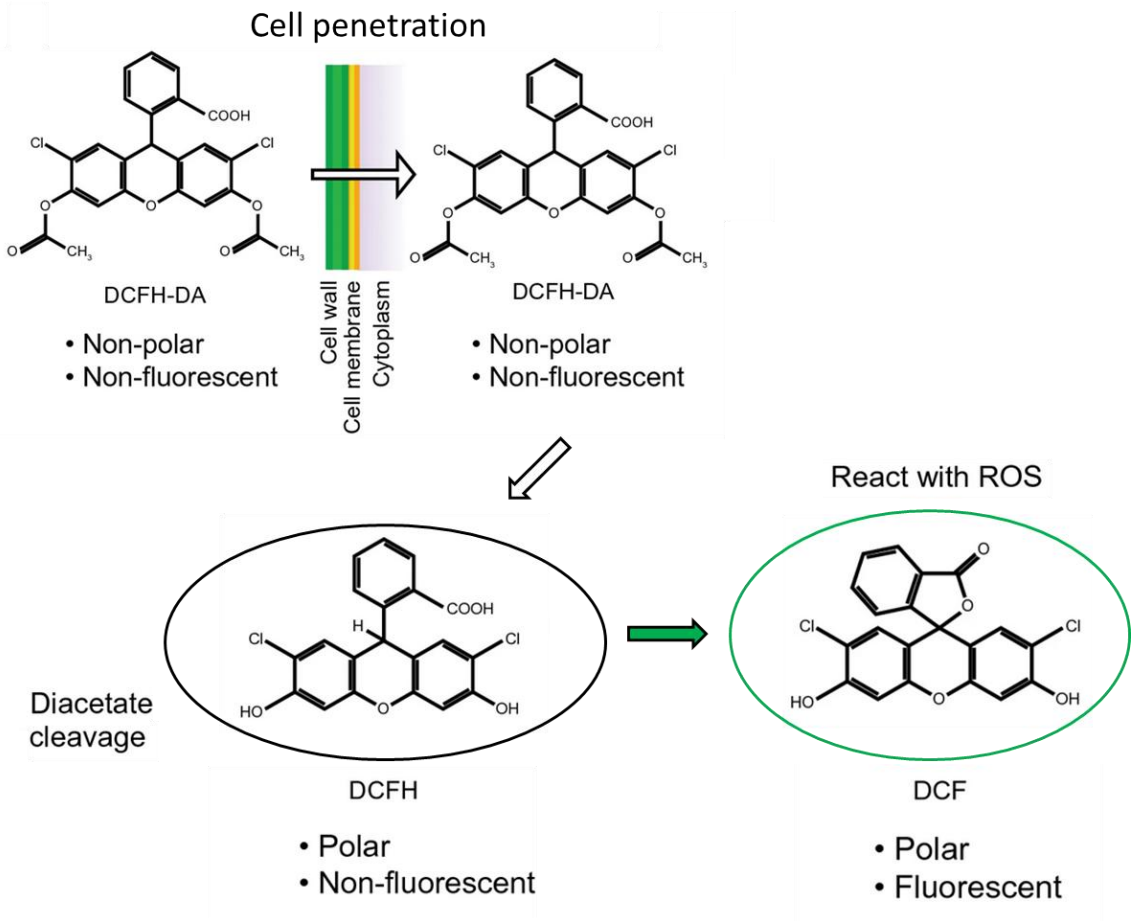

Figure 4.2. Scheme of DCFH-DA action. DCFH-DA is a non-fluorescent compound that, once inside the cell, is deacetylated by cellular esterases into DCFH. After reacting with ROS, DCFH is converted into DCF, which emits green fluorescence. Adapted from [83].

Two conditions were evaluated: (1) acellular ROS production, where ROS generation was measured in NPs diluted in PBS without the presence of cells to assess the impact of NP coating and concentration on ROS formation after irradiation, and (2) intracellular ROS levels, measured after NP treatment and irradiation to determine their effects within the cellular environment.

4.3.5.1 Quantification of acellular ROS production

Acellular ROS production by NPs was evaluated following a protocol adapted from Gerken et al. [84]. Since DCFH-DA does not directly react with ROS, it

must first be hydrolyzed to its deacetylated form, DCFH. In the absence of cells, this conversion requires a strong base, such as NaOH [85 – 87]. To achieve this, DCFH-DA (Sigma-Aldrich) from a 1 mM stock solution was mixed with 0.01 M NaOH at a 1:4 ratio and incubated in the dark for 30 min. To stop the reaction, the mixture was diluted with PBS, resulting in a final solution containing 10 µM DCFH. This solution was used to prepare different concentrations of GNPs or GNP@DX-NH_2 (5, 10, or 20 µg/mL), which were plated in quadruplicates in a 96-well plate (100 µL per well). Two plates were prepared: one served as a non-irradiated control (0 Gy), while the other was irradiated with 6 Gy, and in each plate, a control group containing only DCFH diluted in PBS was also included. Following irradiation, the fluorescence in each well was measured using a Multilabel Plate Reader Platform (Victor X3, model 2030, Perkin Elmer) at an excitation/emission of 485/530 nm. The difference in ROS levels was determined by comparing fluorescence values of the different groups with the non-irradiated PBS control group (0 Gy), and the results were expressed as fold change of fluorescence intensity relative to the non-irradiated PBS control group (0 Gy).

4.3.5.2 Quantification of intracellular ROS production

U87 cells were seeded in 12-well plates at a density of 2.5 x 10^4 cells per well and incubated for 24 h. Then, the cells were treated with 20 µg/mL of GNPs or GNP@DX-NH_2 for 24 h, and irradiated with 2 Gy or 6 Gy. A positive group treated with 200 µM H_2O_2 one hour prior to irradiation was also include, and an additional plate was prepared to evaluate the effects of NP treatment without irradiation (0 Gy). Two hours post-irradiation, the cells were trypsinized, centrifuged (2000 rpm for 5 min), and washed once with PBS. Next, they were incubated at 37°C for 30 min with 10 µM DCFH-DA diluted in PBS. After incubation, cells were centrifuged (2000 rpm for 5 min), resuspended in PBS, and analyzed by flow cytometer (FACS Canto II flow cytometer, Becton Dickinson, EUA) in triplicates (10,000 events per group). The data were quantified using *FlowJo software*. The percentage increase in intracellular ROS levels was calculated by comparing each group with the non-irradiated control group, and the results were expressed as the median fluorescence intensity relative to the 0 Gy control (%).

4.3.6. Statistical analysis

In vitro experiments were performed in triplicate. Results were expressed as the mean or median ± standard deviation. Cytotoxicity results were analyzed for statistical significance by one-way analysis of variance (ANOVA) followed by Tukey's post hoc test. ROS levels were analyzed for statistical significance by ANOVA followed by Dunnett's post-hoc test. Statistical analyses were performed using *GraphPAD® Prism 8.0*, and values of $p < 0.05$ were considered significant.

5. RESULTS AND DISCUSSION

5.1. Characterization of nanoparticles

In this study, GNPs and GNP@DX-NH_2 were synthesized using the co-precipitation method. To evaluate the size distribution and morphology of both nanoparticles, as well as the hydrodynamic diameter and zeta potential, Transmission Electron Microscopy and Dynamic Light Scattering techniques were used. The TEM images obtained are presented in Figure 5.1, along with the size distribution quantified by *ImageJ* software.

GNPs exhibited a core size of approximately 11.9 ± 3.9 nm and presented mostly a spherical morphology (Figures 5.1a and 5.1b). A few elongated NPs were also observed in the images. GNP@DX-NH_2 also presented a rounded morphology but with a smaller core of approximately 8.0 ± 2.5 nm (Figures 5.1c and 5.1d).

The mean hydrodynamic diameter, represented here by both the Z-Average and the mean diameter averaged by number (Dh), as well as the polydispersity index (PDI) and the zeta potential of both NPs are shown in Table 5.1. The PDI indicates the width of the particle size distribution in a suspension, and it ranges from 0.0 to 1.0. A PDI close to 0.0 suggests a narrow size distribution with a homogeneous population of NPs, while a PDI higher than 0.7 indicates a heterogeneous and polydisperse suspension [88]. Table 5.1 also includes the results of GNP@DX and GNP@DX-CL, which represent intermediate steps in the synthesis of GNP@DX-NH_2.

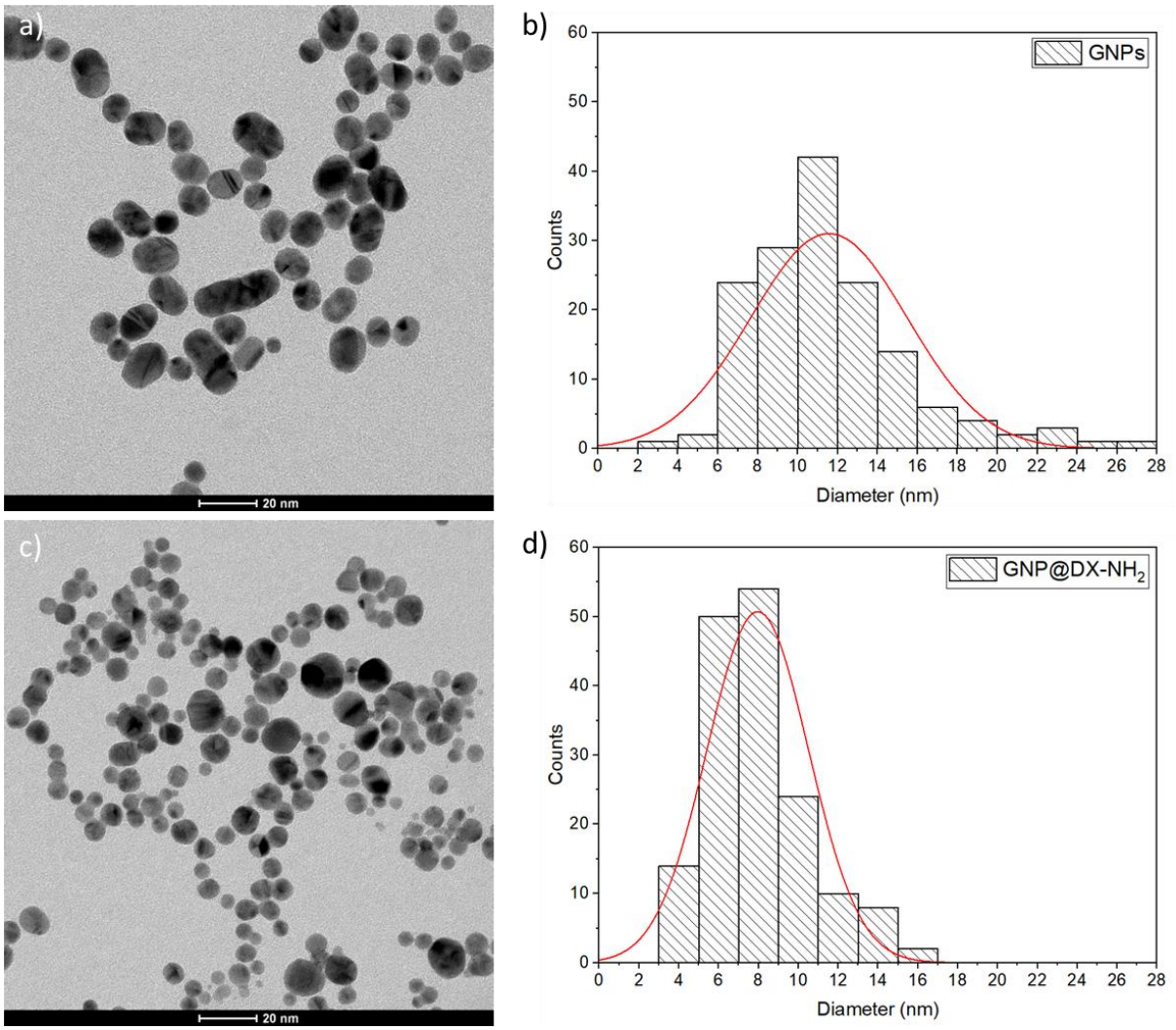

Figure 5.1. Transmission Electron Microscopy images of a) GNPs and c) GNP@DX-NH_2, and histograms representing the size distribution of b) GNPs and d) GNP@DX-NH_2.

Table 5.1. Mean core diameter, hydrodynamic diameter, PDI, and zeta potential of NPs. The core diameter was measured by TEM, while the zeta potential and hydrodynamic diameter were determined by DLS.

Nanoparticle	Core Diameter (nm)	Hydrodynamic diameter (nm)		PDI	Zeta potential (mV)
		Z-average (nm)	Dh (nm)		
GNPs	11.6 ± 3.9	15.8 ± 0.7	0.69 ± 0.02	0.57	- 22.9 ± 0.74
GNP@DX	-	52.48 ± 2.13	3.68 ± 0.95	0.94	-19.0 ± 2.69
GNP@DX-CL	-	84.25 ± 9.51	8.23 ± 3.24	0.98	-28.0 ± 4.85
GNP@DX-NH_2	8.0 ± 2.5	70.70 ± 1.3	37.64 ± 5.64	0.23	- 20.3 ± 0.44

From DLS analysis, GNPs exhibited a mean Z-Average of 15.8 ± 0.7 nm and Dh of 0.69 ± 0.02 nm, with a PDI of 0.57 and a zeta potential of – 22.9 ± 0.7 mV. Interestingly, the Dh extracted from DLS was significantly smaller than the core diameter measured by TEM (11.9 ± 3.9 nm), whereas the Z-Average value was more comparable to TEM measurements. This difference may be attributed to the physical principles of DLS, which determines the diameter of particles based on their mobility within the dispersion medium. Several factors can influence this measurement, including sample concentration, pH, the presence of coatings, or NPs surface functionalization [89 - 91]. Zheng, Bott, and Huo [91] pointed out that gold nanoparticles exhibit size-dependent light scattering properties. Depending on particle size and suspension concentration, multiple scattering events can occur, leading to inaccuracies in the measured average hydrodynamic size.

The measured PDI value of 0.57 indicates a medium-size dispersion, likely due to the presence of elongated GNPs, as observed in Figure 5.1a, or the presence of small NP clusters. Furthermore, the negative zeta potential of –22.9 ± 0,7 mV reflects the presence of BH_4^- and H^- ions, which stabilize the GNPs.

Relative to GNP@DX-NH_2, the protocol for they synthesis was tested and modified by adding a step during the first part of the synthesis. In the original protocol [78], the dextran solution was heated to 80°C before the addition of the chloroauric acid solution. In the modified approach, the dextran solution was heated to 85°C, followed by adding 1M NaOH to increase the pH of the solution before adding the chloroauric acid. This modification was inspired by a comparison of the original protocol with a method proposed by Tang et al. [92] and with a protocol previously used by our group to produce aminated cross-linked iron oxide nanoparticles (CLIO-NH_2) [93].

A comparison of the DLS results for GNP@DX (first synthesis step) and GNP@DX-CL (second synthesis step), shown in Table 5.1, reveals that both the Z-Average and Dh increased, while the zeta potential decreased from -19.0 ± 2.69 mV to -28.0 ± 4.85 mV. This suggests that the epichlorohydrin cross-linking process modified the surface of the NPs. Additionally, even after the cross-linking process,

the PDI of GNP@DX-CL remained high (0.98), possibly indicating the presence of NP clusters.

With the amination process, there was a slight decrease in the Z-average and an increase in the Dh compared to GNP@DX-CL, accompanied by a reduction in the PDI from 0.98 to 0.23. Together, these results suggest a modification of the dextran coating, indicating that the final product (GNP@DX-NH_2) has a narrower size distribution. Moreover, the increase in the zeta potential from -28.0 ± 4.85 mV to -20.3 ± 0.44 mV suggests an alteration in the chemical surface of GNP@DX-NH_2, likely due to the addition of NH_2 groups. Although aminated iron oxide nanoparticles may present a positive zeta potential [93], characteristic of amine groups, the aminated dextran-coated gold nanoparticles prepared by Jang et al. [78] also exhibited a negative zeta potential, shifting from -3.08 mV to -0.76 mV after amination process. Thus, in our case, the negative zeta potential likely indicates a low density of NH_2 groups on the NP surface.

The UV-Vis absorption spectra of both nanoparticles are shown in Figures 5.2. Overall, gold nanoparticles exhibit a characteristic absorption peak between 500 and 550 nm, due to the surface plasmon resonance (SPR) effect [94]. Specifically, spherical gold nanoparticles ranging from 2 to 50 nm typically present a peak around 520 nm, which can shift depending on different factors, such as NP shape, size, and surface modifications [95, 96]. Both GNPs and GNP@DX-NH_2 exhibited absorption peaks within this range, with GNPs showing a peak at approximately 524 nm (Figure 5.2a), while GNP@DX-NH_2 presented a peak at 528 nm (Figure 5.2b). The *in situ* synthesized GNP@DX initially displayed an absorption peak at 516 nm. After the cross-linking process, the peak shifted to 520 nm, and following the amination step, it further increased to 528 nm. These progressive shifts in the absorption peaks throughout the synthesis of GNP@DX-NH_2 align with the DLS analysis, indicating that the cross-linking and amination steps modified the surface structure of GNP@DX.

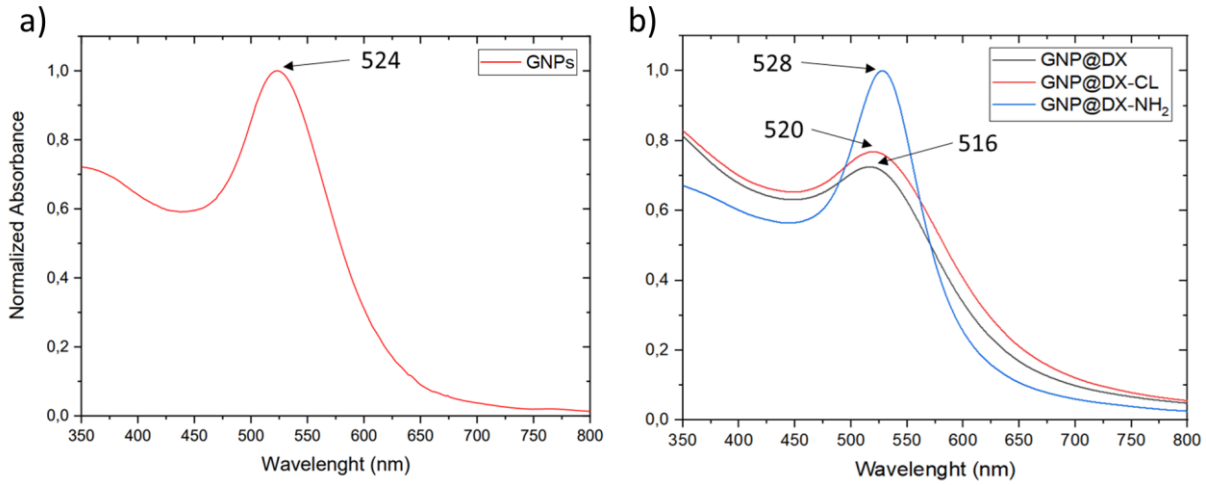

Figure 5.2. UV-Vis absorption peak of a) GNPs at 524 nm and b) GNP@DX (black) at 516 nm, GNP@DX-CL (red) at 520 nm, and GNP@DX-NH_2 (blue) at 528 nm.

TEM, DLS, zeta potential and UV-Vis are techniques commonly used to characterize gold nanoparticles synthesized with different coatings and surface functionalizations. Liu et al. [97] synthesized gold nanoparticles (AuNPs) using sodium borohydride ($NaBH_4$) as a reducing agent, and part of the synthesis was functionalized with borated-protected dopamine dithiocarbamate (B-DDTC). TEM and DLS analyses revealed that unmodified AuNPs had a core size of 6.5 nm and a hydrodynamic diameter of 35.7 nm, while the functionalized B-DDTC-AuNPs had a core of 11.04 nm and a hydrodynamic diameter of 47.3 nm. Additionally, the AuNPs and B-DDTC-AuNPs exhibited a UV-Vis absorption peak at 530 nm and 558 nm, respectively. In another study, Fathy et al. [98] synthesized gold nanoparticles capped with either sodium citrate (Cit-AuNP) or gallic acid (GA-AuNP), which exhibited characteristic UV-Vis absorption peaks at 520 nm and 525 nm, respectively. Furthermore, TEM analysis showed that Cit-AuNP and GA-AuNP had core sizes of approximately 12 nm and 14 nm, and hydrodynamic diameter and zeta potential measurements indicated values of 21 ± 4.1 nm and –16 ± 2.3 mV for Cit-AuNP, and 28.2 ± 6 nm and -11.1 ± 2.6 mV for GA-AuNPs.

Overall, these studies demonstrate that surface functionalization or NP coating leads to measurable changes in their physicochemical properties. Such alterations can be observed through shifts in UV-Vis absorption peaks, variations in hydrodynamic diameter measured by DLS, and changes in zeta potential. Similarly,

these alterations were observed throughout the synthesis steps of GNP@DX-NH_2, where cross-linking and amination of GNP@DX led to progressive changes in UV-Vis absorption peaks and alterations in DLS and zeta potential measurements, highlighting the impact of surface modifications on nanoparticle characterization.

5.2. Nanoparticle cytotoxicity

The effects of GNPs and GNP@DX-NH_2 on the cellular viability of U87, M059J, and Vero cell lines were evaluated by the MTT assay. Cell viability was quantified after 24 h of treatment with different concentrations of NPs, ranging from 5 µg/mL to 50 µg/mL, and the results are shown in Figure 5.3. For Vero cells (Figures 5.3a and 5.3b), concentrations of 20 µg/mL and 50 µg/mL had a significant impact on cell viability compared to the control ($p < 0,05$) for both NPs. Specifically, for GNPs, treatment with 50 µg/mL reduced cell viability below 80%. In contrast, for U87 and M059J, cell viability remained above 80% for both NPs at all concentrations tested.

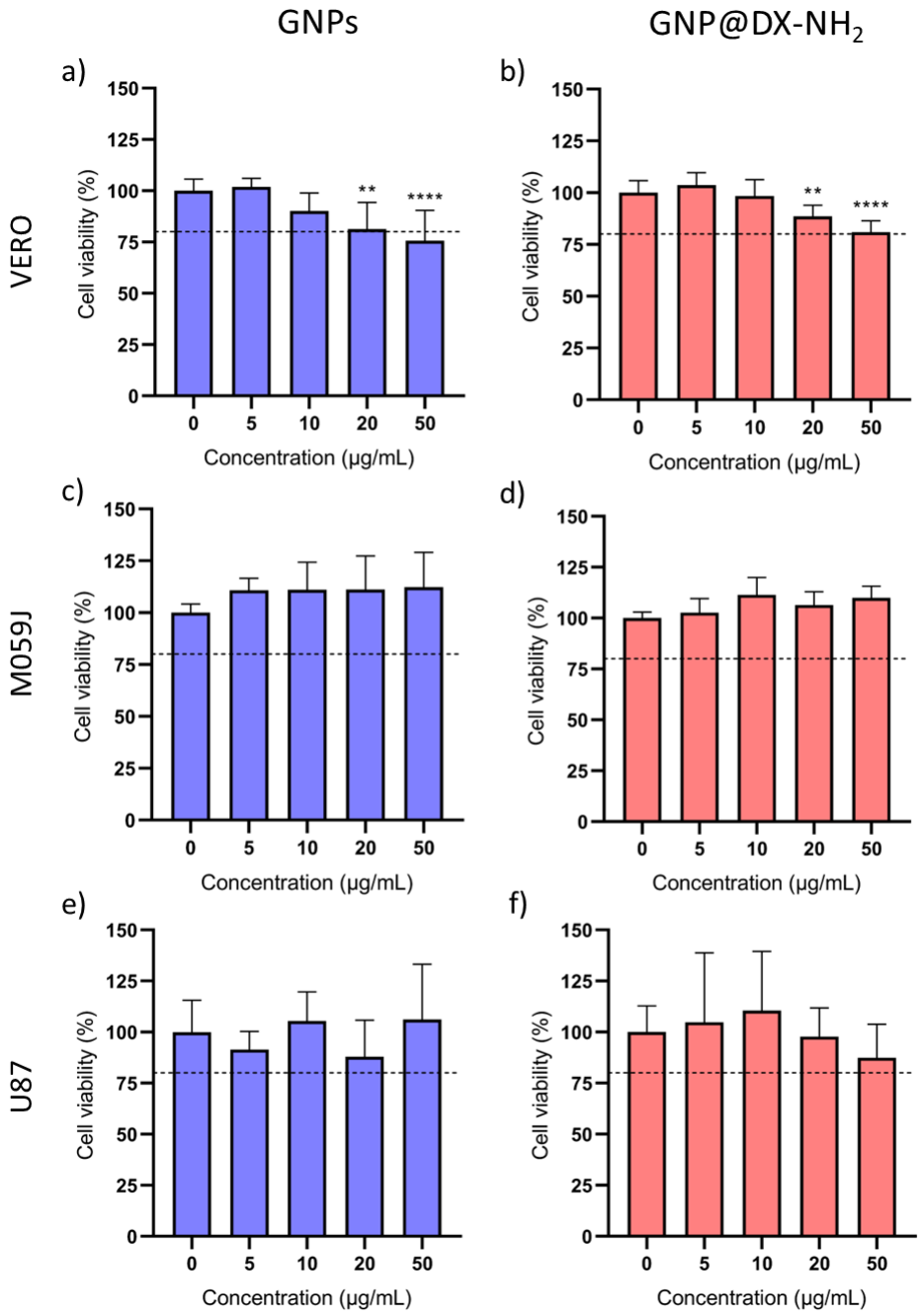

Figure 5.3. Effect of GNPs and GNP@DX-NH_2 on the cell viability of Vero (a, b), M059J (c, d), and U87 (e, f) cell lines. The cell viability was measured after treatment with different concentrations of nanoparticles (0, 5, 10, 20 e 50 µg/ml) for 24h. * Indicates a significant difference compared to the control group. **p ≤ 0.01, ****p ≤ 0.0001.

The cytotoxic effect of NPs depends on several factors, including shape, size, coating, concentration, and the cell line evaluated. Metallic nanoparticles are generally considered non-toxic at low concentrations, and numerous studies have investigated their cytotoxicity. Guerra et al. [45], evaluated the cytotoxicity of GNPs

and dextran-coated SPIONs in U87 and M059J cell lines treated for 24 h with the same concentrations used in this work. Both NPs had no impact on cell viability. In another study, Yang et al. [99] tested Au-Pt NPs coated with PEG in human vascular endothelial (HUEVC) and murine breast cancer (4T1) cell lines. Cells were treated for 24 h with concentrations ranging from 6.25 μg/mL to 200 μg/mL, and no reduction in cell viability was detected. Recently, Fathy et al. [98] compared the effects of citrate- and gallic acid-capped gold nanoparticles (Cit-AuNPs and GA-AuNPs) in HeLa and in Baby Hamster Kidney (BHK) normal cell line. After 24 h of treatment with different concentrations of NPs, the authors found that GA-AuNPs exhibited an IC50 of 91 μg/mL in HeLa cells, while Cit-AuNPs showed a stronger cytotoxic effect, with IC50 of 34 μg/mL. Compared to HeLa cells, both NPs had a similar effect on BHK cells, with IC50 of 52 μg/mL and 45 μg/mL for GA-AuNPs and Cit-AuNPs, respectively.

5.3. Internalization of nanoparticles

The internalization process and cytoplasmic distribution can be affected by several factors, including NP size, shape, and coating material. Furthermore, the internalization of NPs can occur by different mechanisms, including direct penetration through the cellular membrane or endocytosis [100 – 102]. Thus, it is important to evaluate the internalization and cytoplasmic distribution for each NP formulation. Figure 5.4 shows TEM images of U87 cells treated with 20 μg/mL of GNPs (Figures 5.4a and 5.4b) and GNP@DX-NH_2 (Figures 5.4c and 5.4d) for 24 h. NPs are seen as dark spots in the images and are indicated by red arrows. It is possible to see that some NPs are dispersed within the cytoplasm, but the majority are aggregated inside small vesicles randomly distributed throughout the cytoplasm. Some vesicles are located near different organelles, such as mitochondria or the nuclear membrane, but no NPs are observed within the nucleus.

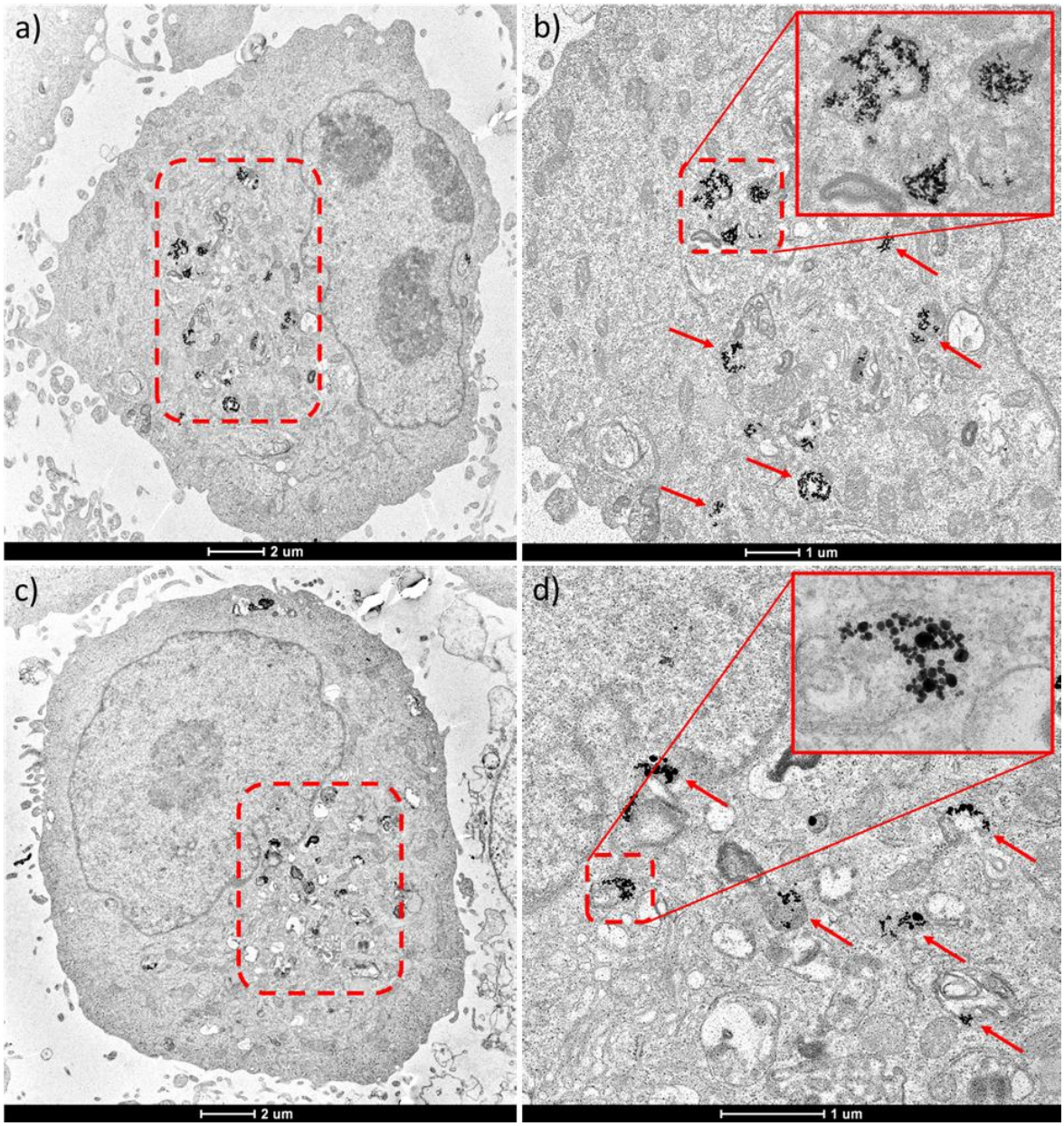

Figure 5.4. Intracellular distribution of NPs in U87 cells after 24 h of treatment with 20 μg/mL of GNPs (a and b) or GNP@DX-NH_2 (c and d).

Similar results were found in different studies. Yue et al. [103] analyzed the cytoplasmatic distribution of three different types of gold nanoparticles coated with small interfering RNA (NP-siRNA) in U87 cells. For the study, they tested 13 nm and 50 nm nanospheres, as well as 40 nm nanostars. After 24 h of incubation, the authors observed that almost all 13 nm NPs remained inside small vesicles, while most of the 50 nm spheres and 40 nm stars formed clusters outside the endosomes, distributed throughout the cytoplasm. In another study, White et al. [104] investigated

the cellular uptake mechanism and the distribution of gold nanorods with a length of approximately 36 nm in SKBR-3 and MCF-7 breast cancer cell lines. The authors found that the NPs were dispersed in the cytoplasm, primarily aggregated inside macropinosomes or lysosomes.

5.4. Production of reactive oxygen species

5.4.1. Quantification of acellular reactive oxygen species production

The production of acellular ROS induced by nanoparticles was quantified using DCFH-DA. Different concentrations of NPs diluted in PBS containing DCFH-DA were prepared, with the control group consisting of a PBS solution without NPs. Two conditions were evaluated: without irradiation (0 Gy) or after irradiation with 6 Gy. The results are shown in Figure 5.5 and are expressed as the fold change of fluorescence intensity relative to the non-irradiated control group (PBS 0 Gy).

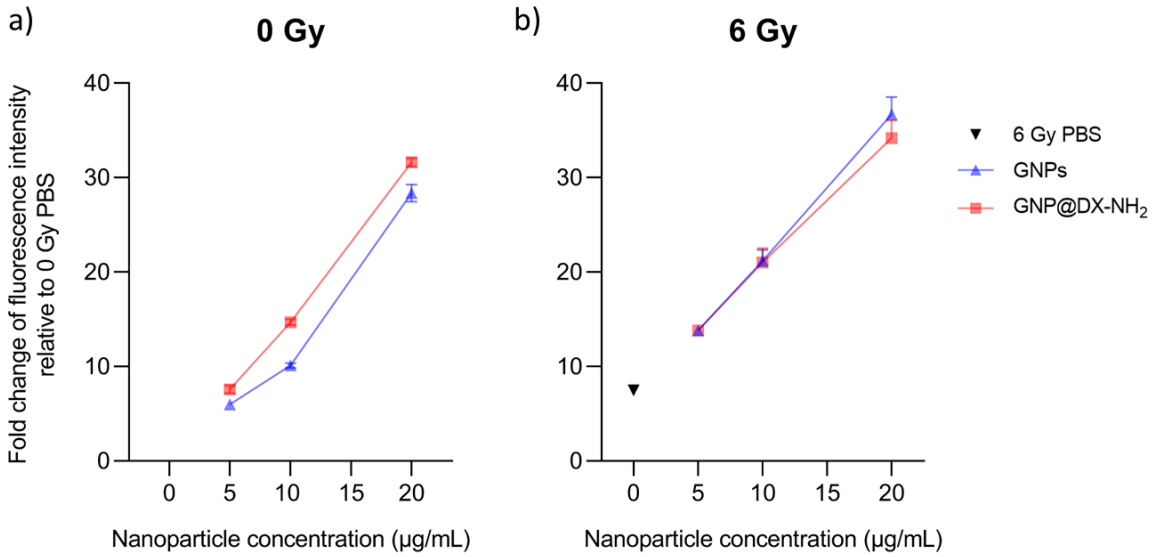

Figure 5.5. Quantification of acellular ROS production induced by GNPs and GNP@DX-NH_2 dispersed in PBS at different concentrations. Results are expressed as fold change of fluorescence intensity relative to non-irradiated PBS control (0 Gy). a) non-irradiated nanoparticles b) irradiated with 6 Gy.

In the non-irradiated group (Figure 5.5a), the presence of nanoparticles induced an increase in ROS levels relative to PBS control. This increase is approximately linear with NP concentration and occurs at similar rates for both NPs.

Without irradiation, GNP@DX-NH_2 generated more ROS than GNPs for all concentrations evaluated. At 20 µg/mL, the difference in ROS levels between the two NPs was approximately 1.12-fold (28.35 and 31.61 for GNPs and GNP@DX-NH_2, respectively). In the irradiated group (Figure 5.5b), both nanoparticles exhibited similar effects, especially at lower concentrations. Unlike the non-irradiated group, GNPs induced a slightly higher ROS production than GNP@DX-NH_2 at 20 µg/mL (36.67 and 34.19, respectively), a difference of 1.07-fold. These results suggest that the coating does may not have an antioxidant effect, as GNP@DX-NH_2 induced ROS levels similar to GNP under both conditions tested.

Finally, a comparison of ROS levels between the irradiated and non-irradiated groups is shown in Figure 5.6. Across all concentrations, GNPs exhibited a greater difference between the irradiated and non-irradiated conditions compared to GNP@DX-NH_2. This difference was more pronounced at 20 µg/mL, where the fold change for non-irradiated GNPs was 28.35, increasing to 36.68 upon irradiation, representing a 1.29-fold increase. In contrast, GNP@DX-NH_2 showed a smaller difference, with a 1.08-fold increase at the same concentration. Furthermore, at 5 µg/mL, both NPs in the non-irradiated group induced ROS levels comparable to those observed in the irradiated PBS group. Overall, the results indicate that both NPs can induce ROS, particularly under irradiation. However, although GNP@DX-NH_2 still generated ROS after irradiation, the comparison between irradiated and non-irradiated groups suggests that the dextran coating mitigates the radiation-induced increase in ROS production, unlike GNPs, which exhibited a more pronounced increase in ROS after irradiation.

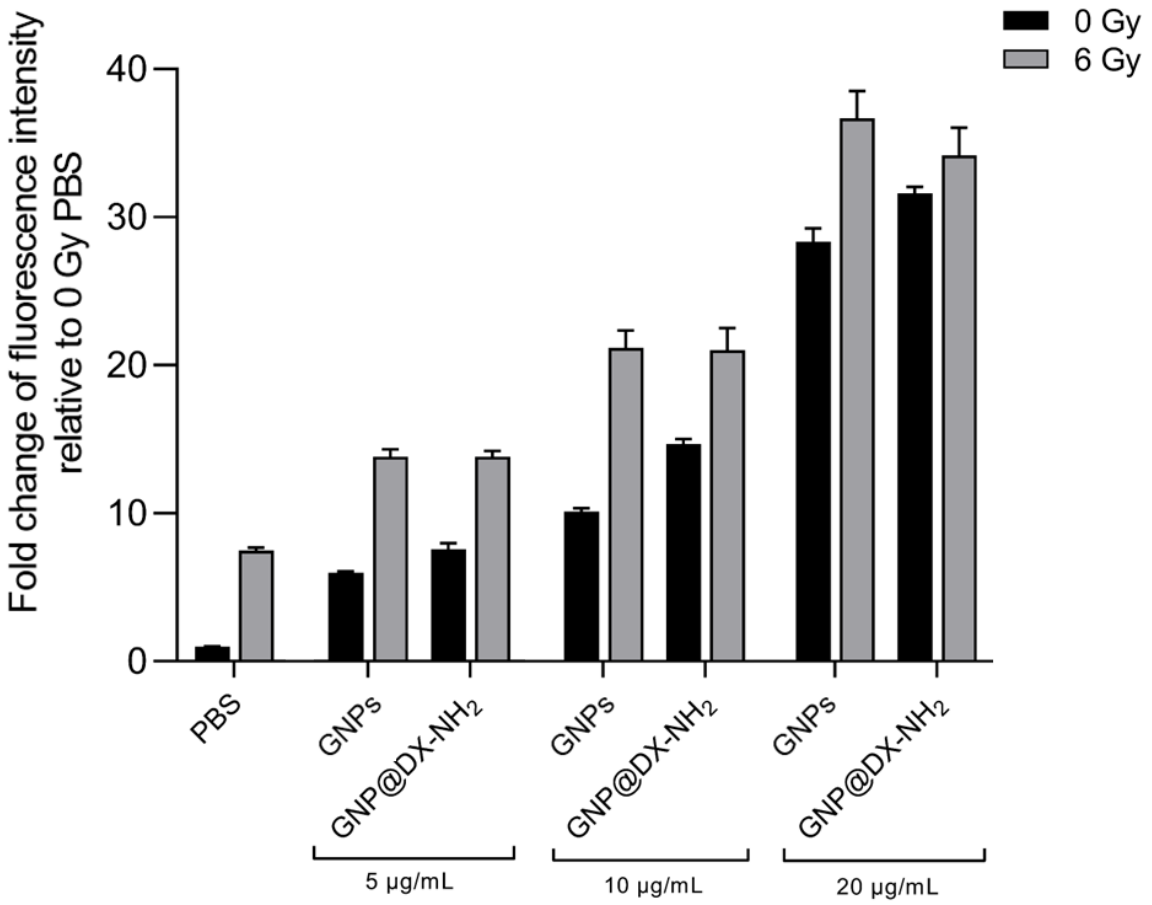

Figure 5.6. Comparison of acellular ROS generation by GNPs and GNP@DX-NH_2 under 0 Gy and 6 Gy. Nanoparticles were diluted in PBS and evaluated at three different concentrations (5, 10, and 20 and µg/mL). Results are expressed as fold change of fluorescence intensity relative to non-irradiated PBS control (0 Gy).

In a similar experiment, Tsai et al. [105] irradiated citrate-capped gold nanoparticles diluted in PBS at different concentrations (20, 40, and 80 ppm) with 0 Gy and 6 Gy using a Cs-137 source. At concentrations of 20 ppm and 40 ppm, irradiated gold nanoparticles induced an increase in ROS production of approximately 32.0- and 39.0-fold, respectively, which aligns with the results found in this study at the concentration of 20 µg/mL.

5.4.2. Quantification of intracellular reactive oxygen species levels

To quantify intracellular ROS levels after irradiation, U87 cells were treated with 20 µg/mL of GNPs or GNP@DX-NH_2 and, after 24 h, irradiated with 2 Gy or 6 Gy. Approximately 2 h post-irradiation, cells were incubated with DCFH-DA, and

ROS levels were quantified by flow cytometry. For this experiment, H_2O_2 was used as a positive control. Figure 5.7 illustrates the fluorescence intensity distribution across different samples, with a grey line added for reference. In comparison to the non-irradiated group (Figure 5.7a), cells exposed to 2 Gy or 6 Gy (Figures 5.7b and 5.7c) exhibited a slight shift in the histogram peaks to the right, indicating an increase in the fluorescence intensity due to elevated ROS levels.

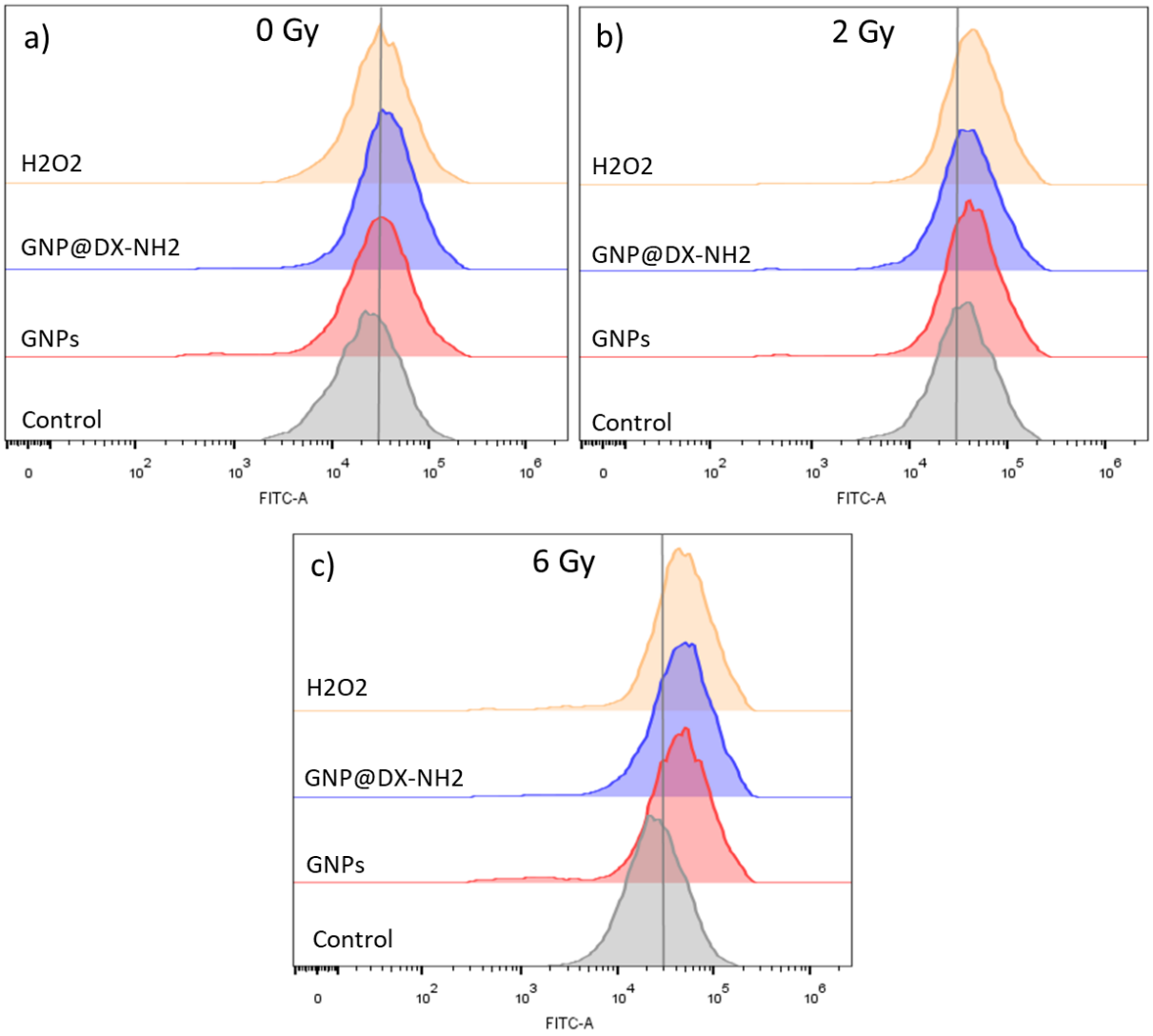

Figure 5.7. Histograms showing the fluorescence intensity distribution of U87 cells treated with GNPs, GNP@DX-NH_2, or H_2O_2 and irradiated with a) 0 Gy, b) 2 Gy, and c) 6 Gy. A shift in the histograms to the right relative to the vertical line is observed across conditions, which indicates an increase in ROS levels.

The median fluorescence intensity for each condition was calculated and expressed as a percentage relative to the 0 Gy control. Figure 5.8 presents the ROS

levels after 24 h of treatment with NPs in the absence of radiation (0 Gy). Compared to the control, both NPs and the positive control showed a significant increase in ROS levels. Treatment with GNP@DX-NH_2 induced higher levels of ROS than GNPs, 54% and 38%, respectively. Although these increases are modest compared to acellular ROS production, GNP@DX-NH_2 induced higher levels of ROS than GNP in both situations.

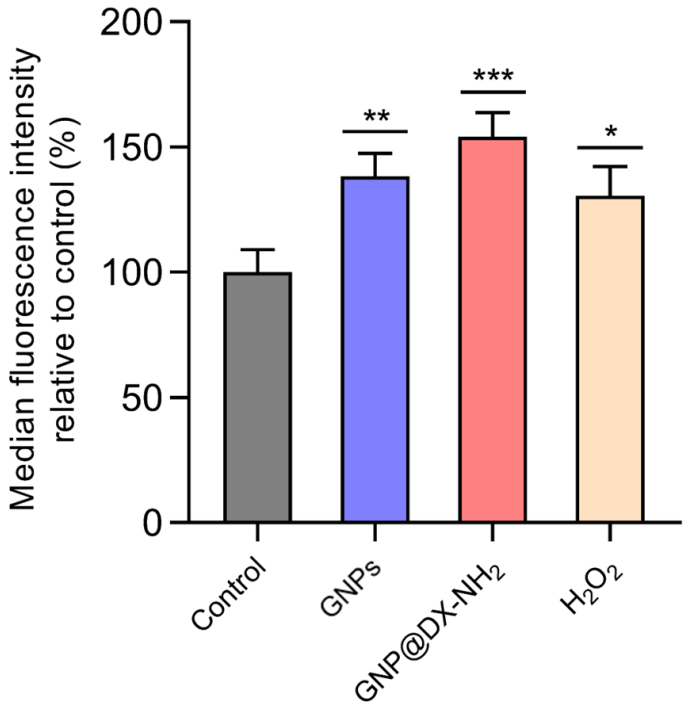

Figure 5.8. Quantification of ROS levels in U87 cells after 24 h of treatment with 20 µg/mL of GNPs or GNP@DX-NH_2. GNPs increased ROS levels by 38%, while GNP@DX-NH_2 induced a 54% increase. The positive control led to a 30% increase. * Indicates a significant difference compared to the control group. *p ≤ 0.05, **p ≤ 0.01, ***p ≤ 0.001.

The median fluorescence intensity of cells treated with nanoparticles and irradiated with 2 Gy or 6 Gy is shown in Figure 5.9, with results presented relative to the 0 Gy control group. Overall, similar ROS levels were expected for both NP treatments following irradiation, with higher levels at 6 Gy. Interestingly, under both irradiation conditions, ROS levels remained constant in GNP-treated groups (69% at 2 Gy and 70% at 6 Gy), whereas GNP@DX-NH_2-treated groups exhibited a notable increase from 60% at 2 Gy to 88% at 6 Gy. Moreover, NPs induced higher levels of ROS than the irradiated control groups at both radiation doses. Contrary to expectations, the control irradiated with 6 Gy exhibited a lower increase in ROS

levels (18%) compared to the control group irradiated with 2 Gy (47%), which may suggest a saturation effect in cellular ROS generation at higher radiation doses.

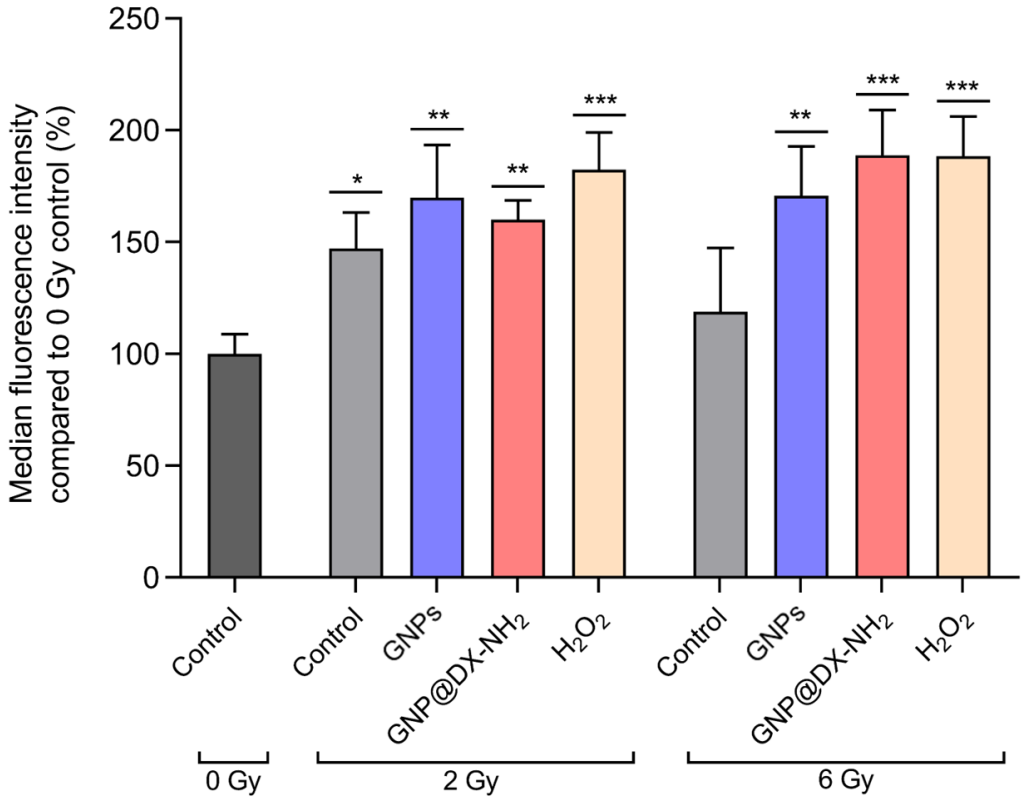

Figure 5.9. Quantification of ROS levels in U87 cells treated with 20 μg/mL of GNPs or GNP@DX-NH_2 for 24 h and irradiated with 2 Gy or 6 Gy. GNPs treatment resulted in similar ROS levels at both radiation doses (69% at 2 Gy and 70% at 6 Gy). GNP@DX-NH_2 induced a 60% increase in ROS levels at 2 Gy, while at 6 Gy, the increase reached 88%. The positive control led to an 88% increase in ROS levels under both radiation conditions. * Indicates a significant difference compared to the 0 Gy control group. *$p \leq 0.05$, **$p \leq 0.01$, ***$p \leq 0.001$.

Considering both irradiated and non-irradiated conditions, GNPs induced a considerable increase in ROS levels after irradiation compared to the non-irradiated GNP group. In contrast, the non-irradiated GNP@DX-NH_2 group already exhibited relatively high ROS levels, showing only a small increase at 2 Gy. However, at 6 Gy, a substantial increase was observed. The difference in ROS levels induced by NPs after irradiation, especially at 6 Gy, may be associated with NP internalization. GNP@DX-NH_2 may be more extensively internalized by cells due to its coating, increasing the chances of interactions with radiation, leading to greater cellular damage. Additionally, elevated ROS levels after radiotherapy may indicate

mitochondrial damage, which can further amplify ROS production and contribute to radiation-induced cytotoxicity [65, 106].

Different studies have investigated the relationship between NPs, ROS production, and mitochondrial damage. Tabatabaie et al. [61] used MitoSox Red to quantify mitochondrial ROS levels at 24 h, 48 h, and 72 h after irradiating human melanoma (MM418) and human prostate cancer (DU148) cell lines with different radiation doses (0, 2, 4, 6, and 8 Gy). The results indicated that the presence of NPs during radiation treatment induced increased mitochondrial damage and ROS production, with a maximum peak of ROS at 4 Gy, which remained significant even 72 h post-irradiation. In another study, Tsai et al. [105] qualitatively evaluated the effects of NPs on ROS levels and mitochondrial damage using fluorescence imaging after irradiation. Human epidermoid carcinoma cells (A431) were treated with gold nanoparticles at a concentration of 80 ppm and irradiated with 6 Gy from a Cs-137 source. The authors observed an increase in cellular ROS levels and a significant decrease in active mitochondria 48 h after irradiation.

Liu et al. [107] evaluated the impact of NP functionalization on ROS generation. HepG2 cells were treated with 10 μg/mL of either polyethylene glycol-capped gold NPs (PEG-AuNPs) or thioctyl tirapazamine-modified gold NPs (TPZs-AuNPs) for 24 h, and ROS levels were quantified after irradiation with 2 Gy or 4 Gy X-rays (50 kVp). Compared to non-irradiated cells, those treated with PEG-AuNP and exposed to 2 Gy or 4 Gy exhibited a significant increase in ROS levels by approximately 1.5- and 2.6-fold, respectively. However, no significant difference was observed between the control and PEG-AuNP-treated groups at the same radiation dose. In contrast, cells treated with TPZs-AuNPs showed a greater increase in ROS of approximately 2- and 3.1-fold at 2 Gy and 4 Gy, respectively, which suggests that the type of nanoparticle coating and functionalization can influence ROS generation and radiosensitization effects.

Overall, results found in the literature vary significantly. ROS generation is a complex process influenced by multiple factors, including NP characteristics (such as material, shape, size, coating, and functionalization), concentration, radiation type and dose, and cellular response. Another critical factor is the methodology used to

quantify ROS levels, as different techniques may vary in sensitivity and specificity. Moreover, cellular ROS levels post-irradiation can fluctuate over time, depending on the extent and location of cellular damage, as well as the activation of repair mechanisms or oxidative stress pathways.

6. CONCLUSION

This study investigated the impact of GNPs and GNP@DX-NH_2 on cell viability and ROS generation in *in vitro* glioblastoma models. Characterization of the synthesized NPs confirmed that both had a small spherical core (~10 nm), and zeta potential and UV-vis data verified the surface modification and the presence and amination of the dextran coating in GNP@DX-NH_2.

Cytotoxicity assays demonstrated that neither GNP nor GNP@DX-NH_2 induced toxic effects or significantly reduced the viability of U87 and M059J cells. However, in Vero cells, used as a normal tissue control, GNPs at 50 µg/mL reduced viability below 80%. TEM analysis revealed that both NPs were internalized and localized within vesicles distributed throughout the cytoplasm, often near organelles such as mitochondria. However, no nanoparticles were observed in the nucleus.

The results demonstrated that both NPs influenced ROS levels, with distinct effects depending on the radiation dose and nanoparticle coating. GNPs treatment led to a pronounced increase in ROS levels after irradiation compared to the non-irradiated condition, although ROS levels remained similar between radiation doses. Meanwhile, the GNP@DX-NH2-treated group exhibited relatively high ROS levels even in the absence of radiation, with a moderate increase at 2 Gy and a substantial effect at 6 Gy.

The literature review reinforced the complexity of nanoparticle-mediated radiosensitization, highlighting the influence of multiple factors on ROS production. Studies using different cellular models and radiation sources consistently report an increase in ROS levels upon nanoparticle exposure, often associated with mitochondrial damage and oxidative stress. However, variations in experimental conditions and ROS quantification methodologies present challenges in directly

comparing findings and establishing a standardized framework for nanoparticle-based radiosensitization strategies.

Further studies are needed to enhance statistical robustness, to allow a more precise evaluation of the observed effects, and to elucidate the precise molecular mechanisms underlying nanoparticle-induced ROS generation. Moreover, quantifying nanoparticle internalization could help determine whether the dextran coating directly enhances ROS production or merely increases nanoparticle uptake, leading to higher intracellular GNP@DX-NH_2 levels and a greater likelihood of interaction with radiation.

Overall, this study contributes to the understanding of the role of nanoparticle functionalization in modulating ROS production and radiosensitization. While the findings highlight the potential of gold nanoparticles in glioblastoma treatment, further investigations are needed to optimize nanoparticle formulations, evaluate their long-term effects, and elucidate the mechanisms underlying their interaction with radiation. By addressing these aspects, future research may pave the way for improved nanoparticle-based radiosensitization strategies, ultimately enhancing therapeutic outcomes in glioblastoma treatment.

7. FUTURE STUDIES

Future studies are necessary to further investigate the radiosensitization effects induced by dextran-coated gold nanoparticles. Regarding the physicochemical properties, additional characterization techniques that couldn't be done in this work should be employed. The evaluation of the dextran coating mass could be conducted using thermogravimetric analysis (TGA), while the characterization of the metallic core could be performed through X-ray diffraction analysis (XRD).

Regarding biological effects, several experiments could be conducted. First, quantification of nanoparticle internalization using inductively coupled plasma mass spectrometry (ICP-MS) would help to determine whether the dextran coating increases NP uptake. This data could then be correlated with the increase in ROS levels after irradiation to establish a clearer relationship between intracellular NP concentration and oxidative stress.

The dynamics of ROS generation could also be more extensively studied. A good approach would be to measure ROS levels 2 or 3 h after irradiation and again after 24 h to assess whether they return to basal levels. Additionally, quantifying mitochondrial damage at 24 h and 48 h post-irradiation would help to determine whether ROS production is linked to mitochondrial dysfunction over time.

Other assays could provide further insights, such as the clonogenic assay to evaluate the efficacy of NP-induced radiosensitization, apoptosis and necrosis assays to determine the activation of different cell death pathways, and cell cycle analysis to assess potential cell cycle arrest. Furthermore, the study could also be extended to other glioblastoma cell lines, such as U251 and M059J.

8. REFERENCES

[1] Cancer. **World Health Organization.** 3 feb. 2022. Available at: https://www.who.int/news-room/fact-sheets/detail/cancer.

[2] Ferlay, J. et al. Global cancer observatory: cancer today. Int. Agency Res. **Cancer,** (2020).

[3] Tan, Aaron C. et al. Management of glioblastoma: State of the art and future directions. **CA: A Cancer Journal for Clinicians**, v. 70, n. 4, p. 299–312, 2020. Doi: 10.3322/caac.21613.

[4] Wen, Patrick Y. et al. Glioblastoma in adults: A Society for Neuro-Oncology (SNO) and European Society of Neuro-Oncology (EANO) consensus review on current management and future directions. **Neuro-oncology,** v. 70, n. 8, p. 1073-1113, aug. 2020. Doi:10.1093/neuonc/noaa106.

[5] Symonds, Paul; Mills, John; Duxbury, Angela. **Walter and Miller's Textbook of Radiotherapy: Radiation Physics, Therapy and Oncology**. 8ª ed. Philadelphia: Elsevier, 2019. 640p.

[6] Oronsky, Bryan et al. A Review of Newly Diagnosed Glioblastoma. **Frontiers in Oncology**, vol. 10, p. 574012, 2021. doi:10.3389/fonc.2020.574012.

[7] Hanif, Farina et al. Glioblastoma multiforme: A review of its epidemiology and pathogenesis through clinical presentation and treatment. **Asian Pacific Journal of Cancer Prevention**, vol. 18, n. 1, p. 3-9, 2017. Doi: 10.22034/APJCP.2017.18.1.3.

[8] Carvalho, Juliana A. D. V. et al. Systemic dissemination of glioblastoma: literature review, **Rev. Assoc. Med. Bras**., vol. 65, n. 3, p. 460-468, mar. 2019. Doi: 10.1590/1806-9282.65.3.460.

[9] Tepper, Joel E.; Foote, Robert L; Michalsky, Jeff M. **Gunderson and Tepper's Clinical Radiation Oncology.** 5ª ed. Philadelphia: Elsevier, 2019. 1656p.

[10] Gong, Liuyun et al. Application of Radiosensitizers in Cancer Radiotherapy. **International journal of nanomedicine**, vol. 16, p. 1083-1102, feb. 2021. Doi: 10.2147/IJN.S290438.

[11] Martínez-Torres, Ana Carolina et al. Chitosan gold nanoparticles induce cell death in HeLa and MCF-7 cells through reactive oxygen species production. **International journal of nanomedicine**, v. 13, p. 3235-3250, may. 2018. Doi: 10.2147/IJN.S165289.

[12] Shariatzadeh, Siavash et al. Metallic Nanoparticles for the Modulation of Tumor Microenvironment: A New Horizon. **Frontiers in bioengineering and biotechnology**, v. 10, feb. 2022. Doi: 10.3389/fbioe.2022.847433.

[13] Khursheed, Rubiya et al. Biomedical applications of metallic nanoparticles in cancer: Current status and future perspectives. **Biomedicine & pharmacotherapy**, v. 150, p. 112951, apr. 2022. Doi: 10.1016/j.biopha.2022.112951.

[14] Sharma, Ankush; Goyal, Amit K.; Rath, Goutam. Recent advances in metal nanoparticles in cancer therapy. **Journal of drug targeting**, v. 26, n. 8, p. 617-632, 2018. Doi: 10.1080/1061186X.2017.1400553.

[15] Penninckx, Sébastien; Heuskin, Anne-Catherine; Michiels, Carine; Lucas, Stéphane. Gold Nanoparticles as a Potent Radiosensitizer: A Transdisciplinary Approach from Physics to Patient. **Cancers**, v. 12, n. 8, p. 2021, jul. 2020. Doi:10.3390/cancers12082021.

[16] Jia, Shichong et al. Promoting reactive oxygen species generation: a key strategy in nanosensitizer-mediated radiotherapy. **Nanomedicine**, vol. 16, n. 9, p. 759-778, 2021. Doi:10.2217/nnm-2020-0448.

[17] Howard, Douglas et al. Chemical Mechanisms of Nanoparticle Radiosensitization and Radioprotection: A Review of Structure-Function Relationships Influencing Reactive Oxygen Species. **International journal of molecular sciences**, v. 21, n. 2, p. 579, jan. 2020. Doi:10.3390/ijms21020579.

[18] Getting External Beam Radiation Therapy. **American Cancer Society**. 10 apr. 2022. Available at: https://www.cancer.org/treatment/treatments-and-side-effects/treatment-types/radiation/external-beam-radiation-therapy.html.

[19] Saha, Gopal B.; **Physics and Radiobiology of Nuclear Medicine.** 4ª ed. New York: Springer, 2013. 320p.

[20] Turner, James E.; **Atoms, Radiation and Radiation Protection.** 3ª ed. Darmstadt: Wiley-Vch, 2007. 606p.

[21] Murshed, Hasan. **Fundamentals of radiation oncology: physical, biological, and clinical aspects**. 3ª ed. Massachusetts: Academic Press, 2019. 713p.

[22] Rangacharyulu, Chary. **Physics of Nuclear Radiations: Concepts, Techniques and Applications**. 1ª ed. Florida: CRC Press, 2014. 383p.

[23] Shani, Gad. **Radiation Dosimetry: Instrumentation and Methods.** 2ª ed. Florida: CRC Press, 2000. 456p

[24] Tabakov, Slavik; Milano, Franco; Strand, Sven-Erik; Lewis, Cornelius; Sprawls, Perry. **Encyclopedia of Medical Physics: Volume I and II**. 1ª ed. Florida: CRC Press, 2013. 908p.

[25] DeVita, Vincent T., Jr; Lawrence, Theodore S.; Rosenberg, Steven A. **DeVita, Hellman, and Rosenberg's Cancer: Principles & Practice of Oncology.** 11ª ed. Philadelphia: Wolters Kluwer, 2019. 2638p.

[26] Podgorsak, E. B. **Radiation Oncology Physics: A Handbook for Teachers and Students**. 1ª ed. Vienna: Internacional Atomic Energy Agency, 2005. 657p.

[27] Tubiana, Maurice; Dutreix, Jean; Wambersie, André. **Introduction to radiobiology.** 1ª ed. London: Taylor & Francis Group, 1990. 261p.

[28] Azzam, Edouard I.; Jay-Gerin, Jean-Paul; Pain, Debkumar. Ionizing Radiation-Induced Metabolic Oxidative Stress and Prolonged Cell Injury. **Cancer Letters**, vol. 327, n. 1-2, p. 48-60, 2012. Doi:10.1016/j.canlet.2011.12.012.

[29] Bushberg, Jerrold T.; Seibert, J. Anthony; Leidholdt Jr., Edwin M.; Boone, John M. **The Essential Physics of Medical Imaging**. 3ª ed. 2011. Philadelphia: Lippincott Williams & Wilkins, 2012. 1048p.

[30] Cuyper, Marcel; Bulte, Jeff W. M. **Physics and Chemistry Basis of Biotechnology**. 1ª ed. Philadelphia: Elsevier, 2001. 334p.

[31] Baby, Rabia et al. Nanomaterials for the Treatment of Heavy Metal Contaminated Water. **Polymers**, v. 14, n. 3, p. 538, jan. 2022. Doi: 10.3390/polym14030583.

[32] Lin, Yingzheng et al. Engineering Noble Metal Nanomaterials for Pollutant Decomposition. **Industrial & Engineering Chemistry Research**, v. 59, n. 47, p. 20561-20581, nov. 2020. Doi: 10.1021/acs.iecr.0c04258.

[33] Rai, Prabhakar. Plasmonic noble metal@metal oxide core–shell nanoparticles for dye-sensitized solar cell applications. **Sustainable Energy Fuels**, v. 3, n. 1, p. 63-91, 2019. Doi: 10.1039/C8SE00336J.

[34] Yao, Kai et al. Plasmonic Metal Nanoparticles with Core-Bishell Structure for High-Performance Organic and Perovskite Solar Cells. **ACS nano**, v. 13, n. 5, p. 5397-5409, 2019. Doi: 10.1021/acsnano.9b00135.

[35] Yang, W. et al. Shape effects of gold nanoparticles in photothermal cancer therapy. **Materials Today Sustainability**, v. 13, p. 100078, sep. 2021. Doi: 10.1016/j.mtsust.2021.100078.

[36] Poklepovich-Caride, Santiago et al. A versatile one-pot room temperature approach for the synthesis of gold nanoparticles with multiple sizes and shapes. **Colloids and Surfaces A: Physicochemical and Engineering Aspects**, v. 646, p. 128890, aug. 2022. Doi: 10.1016/j.colsurfa.2022.128890.

[37] Raghunathan, Karthik et al. Tuning and tracking the growth of gold nanoparticles synthesized using binary surfactant mixtures. **Nanoscale advances**, v. 2, n. 5, p. 1980-1992, mar. 2020. Doi: 10.1039/d0na00214c.

[38] Cole, Lisa E. et al. Gold nanoparticles as contrast agents in x-ray imaging and computed tomography. **Nanomedicine**, v. 10, n. 2, p. 321-41, 2015. Doi: 10.2217/nnm.14.171.

[39] Ramírez-Nava, Gerardo et al. Hybrid (2D/3D) Dosimetry of Radiolabeled Gold Nanoparticles for Sentinel Lymph Node Detection in Patients with Breast Cancer. **Contrast media & molecular imaging**, v. 2020, n. 2728134, may. 2020. Doi: 10.1155/2020/2728134.

[40] Silva, Francisco; Campello, Maria P. C; Paulo, António. Radiolabeled Gold Nanoparticles for Imaging and Therapy of Cancer. **Materials**, v. 14, n. 1, dec. 2020. Doi: 10.3390/ma14010004.

[41] García-Álvarez, Rafaela et al. Optimizing the Geometry of Photoacoustically Active Gold Nanoparticles for Biomedical Imaging. **ACS Photonics**, v. 7, n. 3, p. 646-652, 2020. Doi: 10.1021/acsphotonics.9b01418.

[42] Nguyen, V.P. et al. Chain-like gold nanoparticle clusters for multimodal photoacoustic microscopy and optical coherence tomography enhanced molecular imaging. **Nature Communications**, v. 12, n. 34, 2021. Doi: 10.1038/s41467-020-20276-z.

[43] Amina, Sundus J.; Guo, Bin. A Review on the Synthesis and Functionalization of Gold Nanoparticles as a Drug Delivery Vehicle. **International journal of nanomedicine,** v. 15, p. 9823-9857, dec. 2020. Doi: 10.2147/IJN.S279094.

[44] Li, Dongdong et al. GMT8 aptamer conjugated PEGylated Ag@Au core-shell nanoparticles as a novel radiosensitizer for targeted radiotherapy of glioma. **Colloids and Surfaces B: Biointerfaces**, v. 211, p. 112330, mar. 2022. Doi: 10.1016/j.colsurfb.2022.112330.

[45] Guerra, Danieli B. et al. Intercomparison of radiosensitization induced by gold and iron oxide nanoparticles in human glioblastoma cells irradiated by 6 MV photons. **Scientific Reports**, v. 12, n. 1, p. 1-11, 2022. Doi: 10.1038/s41598-022-13368-x.

[46] Minaei, Soraya Emamgholizadeh et al. Sensitization of glioblastoma cancer cells to radiotherapy and magnetic hyperthermia by targeted temozolomide-loaded magnetite tri-block copolymer nanoparticles as a nanotheranostic agent. **Life sciences**, vol. 306, p. 120729, oct. 2022. Doi: 10.1016/j.lfs.2022.120729.

[47] Zainudin, Nur Hamizah Mohd et al. Cellular analysis on the radiation induced bystander effects due to bismuth oxide nanoparticles with 6 MV photon beam radiotherapy. **Journal of Radiation Research and Applied Sciences**, v. 15, n. 3, p. 318-325, sep. 2022. Doi: 10.1016/j.jrras.2022.08.003.

[48] Tudda, Alessia et al. Breast radiotherapy with kilovoltage photons and gold nanoparticles as radiosensitizer: An in vitro study. **Medical physics**, v. 49, n. 1, p. 568-578, 2022. Doi:10.1002/mp.15348.

[49] Hullo, Marie et al. Radiation Enhancer Effect of Platinum Nanoparticles in Breast Cancer Cell Lines: In Vitro and In Silico Analyses. **International journal of molecular sciences**, v. 22, n. 9, p. 4436, Apr. 2021. Doi:10.3390/ijms22094436.

[50] Arab-Bafrani, Zahra et al. Enhanced radiotherapy efficacy of breast cancer multi cellular tumor spheroids through in-situ fabricated chitosan-zinc oxide bio-nanocomposites as radio-sensitizing agents. **International Journal of Pharmaceutics**, v. 605, p. 120828, aug. 2021. Doi:10.1016/j.ijpharm.2021.120828.

[51] Ahmad, Reem et al. Radiobiological Implications of Nanoparticles Following Radiation Treatment. **Particle & Particle Systems Characterization**, v. 37, n. 4, p. 1900411, mar. 2020. Doi:10.1002/ppsc.201900411.

[52] Samani, Roghayeh Kamran et al. Trastuzumab and folic acid functionalized gold nanoclusters as a dual-targeted radiosensitizer for megavoltage radiation therapy of human breast cancer. **European Journal of Pharmaceutical Sciences**, v. 153, p. 105487, oct. 2020. Doi: 10.1016/j.ejps.2020.105487.

[53] Zangeneh, Masoumeh et al. Enhanced cytotoxic and genotoxic effects of gadolinium-doped ZnO nanoparticles on irradiated lung cancer cells at megavoltage radiation energies. **Materials Science and Engineering: C**, v. 103, p. 109739, oct. 2019. Doi: 10.1016/j.msec.2019.109739.

[54] Rashid, Raizulnasuha Abdul et al. Radiosensitization effects and ROS generation by high Z metallic nanoparticles on human colon carcinoma cell (HCT116) irradiated under 150 MeV proton beam. **OpenNano**, v. 4, p. 100027, 2019. Doi: 10.1016/j.onano.2018.100027.

[55] Darfarin, Ghazal et al. The effect of SiO2/Au core-shell nanoparticles on breast cancer cell's radiotherapy. **Artificial Cells, Nanomedicine, and Biotechnology**, v. 46, n. sup2, p. 836-846, 2018. doi:10.1080/21691401.2018.1470526.

[56] Davidi, Erez Shmuel et al. Cisplatin-conjugated gold nanoparticles as a theranostic agent for head and neck cancer. **Head & neck**, v. 40, n. 1, p. 70-78, 2018. Doi:10.1002/hed.24935.

[57] Rosa, Soraia et al. Biological mechanisms of gold nanoparticle radiosensitization. **Cancer nanotechnology**, vol. 8, n. 1, p. 1-25, feb. 2017. Doi: 10.1186/s12645-017-0026-0.

[58] Abolfazli, Khadem et al. Studying Effects of Gold Nanoparticle on Dose Enhancement in Megavoltage Radiation. **Journal of biomedical physics & engineering**, vol. 5, n. 4, p. 185-190, Dec. 2015.

[59] Alamzadeh, Zahra et al. Gold nanoparticles promote a multimodal synergistic cancer therapy strategy by co-delivery of thermo-chemo-radio therapy. **European Journal of Pharmaceutical Sciences**, v. 145, p. 105235, mar. 2020. Doi: 10.1016/j.ejps.2020.105235.

[60] Du, Chengrun et al. AntiPD-L1 antibody conjugated Au-SPIOs nanoplatform for enhancing radiosensitivity and triggering anti-tumor immune response. **Scientific reports**, v. 12, n. 1, p. 19542, nov. 2022. Doi:10.1038/s41598-022-23434-z.

[61] Tabatabaie, Farnaz; Franich, Rick; Feltis, Bryce; Geso, Moshi. Oxidative Damage to Mitochondria Enhanced by Ionising Radiation and Gold Nanoparticles in Cancer Cells. **International journal of molecular sciences**, v. 23, n. 13, p. 6887, jun. 2022. Doi:10.3390/ijms23136887.

[62] Sicard-Roselli, Cécile et al. A new mechanism for hydroxyl radical production in irradiated nanoparticle solutions. **Small**, vol. 10, n. 16, p. 3338-3346, may 2014. Doi: 10.1002/smll.201400110.

[63] Mikami, Yusuke; Dhakshinamoorthy, Amarajothi; Alvaroa, Mercedes; García, Hermenegildo. Catalytic activity of unsupported gold nanoparticles. **Catalysis Science & Technology**, v. 3, n. 1, p. 58-69, 2013. Doi: 10.1039/C2CY20068F.

[64] Choi, By J. et al. A gold nanoparticle system for the enhancement of radiotherapy and simultaneous monitoring of reactive-oxygen-species formation. **Nanotechnology**, v. 29, n. 50, p. 504001, 2018. Doi:10.1088/1361-6528/aae272.

[65] Kim, Wanyeon et al. Cellular Stress Responses in Radiotherapy. **Cells**, vol. 8, n. 9, p. 1105, sep. 2019. Doi:10.3390/cells8091105.

[66] Pinel, Sophie et al. Approaches to physical stimulation of metallic nanoparticles for glioblastoma treatment. **Advanced drug delivery reviews**, vol. 138, p. 344-357, 2019. Doi:10.1016/j.addr.2018.10.013.

[67] Štefančíková, Lenka et al. Effect of gadolinium-based nanoparticles on nuclear DNA damage and repair in glioblastoma tumor cells. **Journal of nanobiotechnology**, v. 14, n. 1, jul. 2016. Doi:10.1186/s12951-016-0215-8.

[68] Marill, Julie; Anesary, Naeemunnisa Mohamed; Paris, Sébastien. DNA damage enhancement by radiotherapy-activated hafnium oxide nanoparticles improves cGAS-STING pathway activation in human colorectal cancer cells. **Radiotherapy and Oncology**, v. 141, p. 262-266, 2019. Doi: 10.1016/j.radonc.2019.07.029.

[69] Yogo, Katsunori et al. Radiosensitization Effect of Gold Nanoparticles on Plasmid DNA Damage Induced by Therapeutic MV X-rays. **Nanomaterials**, v. 12, n. 5, p. 771, feb. 2022. Doi: 10.3390/nano12050771.

[70] Matthews, Helen K.; Bertoli, Cosetta; De Bruin, Robertus A. M. Cell cycle control in cancer. **Nature Reviews Molecular Cell Biology**, v. 23, n. 1, p. 74-88, 2022. Doi: 10.1038/s41580-021-00404-3.

[71] Lee, Dong Gun et al. Gold nanoparticles conjugated with resveratrol induce cell cycle arrest in MCF-7 cell lines. **Applied Biological Chemistry**, v. 62, n. 1, p. 1-6, 2019. Doi: 10.1186/s13765-019-0440-6.

[72] Ren, Yuanyuan et al. Involvement of TGF-β and ROS in G1 Cell Cycle Arrest Induced by Titanium Dioxide Nanoparticles Under UVA Irradiation in a 3D Spheroid Model. **International journal of nanomedicine**, v. 15, p. 1997-2010, mar. 2020. Doi:10.2147/IJN.S238145.

[73] Li, Qian; Huang, Chun; Liu, Liwei; Hu, Rui; Quet, Junle. Effect of Surface Coating of Gold Nanoparticles on Cytotoxicity and Cell Cycle Progression. **Nanomaterials**, v. 8, n. 12, p. 1063, dec. 2018. Doi:10.3390/nano8121063.

[74] Şimşek, Sinem et al. DNA-damage and cell cycle arrest initiated anti-cancer potency of super tiny carbon dots on MCF7 cell line. **Scientific reports**, v. 10, n. 1, p. 13880, aug. 2020. Doi:10.1038/s41598-020-70796-3.

[75] Abdel-Ghany, Shaimaa et al. Gold nanoparticles induce G2/M cell cycle arrest and enhance the expression of E-cadherin in breast cancer cells. **Inorganic and Nano-Metal Chemistry**, v. 50, n. 10, p. 926-932, 2020. Doi:10.1080/24701556.2020.1728553.

[76] Gioria, Sabrina et al. A proteomic approach to investigate AuNPs effects in Balb/3T3 cells. **Toxicology letters**, v. 228, n. 2, p. 111-126, 2014. Doi: 10.1016/j.toxlet.2014.04.016.

[77] Perillo, Bruno et al. ROS in cancer therapy: the bright side of the moon. **Experimental & molecular medicine**, vol. 52, n.2, p. 192-203, 2020. Doi:10.1038/s12276-020-0384-2.

[78] Jang, Hongje et al. The effective nuclear delivery of doxorubicin from dextran-coated gold nanoparticles larger than nuclear pores. **Biomaterials,** vol. 34, n. 13, p. 3503-3510, apr. 2013. Doi: 10.1016/j.biomaterials.2013.01.076.

[79] Ghasemi, Mahshid et al. The MTT assay: utility, limitations, pitfalls, and interpretation in bulk and single-cell analysis. **International journal of molecular sciences**, v. 22, n. 23, p. 12827, 2021. Doi: 10.3390/ijms222312827.

[80] Yu, Daliang et al. Improved detection of reactive oxygen species by DCFH-DA: New insight into self-amplification of fluorescence signal by light irradiation. **Sensors and Actuators B: Chemical**, v. 339, p. 129878, 2021. Doi: 10.1016/j.snb.2021.129878.

[81] Setsukinai, K. ichi, Urano Y, Kakinuma K, Majima HJ, Nagano T. Development of novel fluorescence probes that can reliably detect reactive oxygen species and distinguish specific species. **J Biol Chem**, v. 278, p. 3170-3175, 2003. Doi: 10.1074/jbc.M209264200.

[82] Gomes, Ana; Fernandes, Eduarda; Lima, José LFC. Fluorescence probes used for detection of reactive oxygen species. **Journal of biochemical and biophysical methods**, v. 65, n. 2-3, p. 45-80, 2005. Doi: 10.1016/j.jbbm.2005.10.003.

[83] Ezequiel, João et al. Concurrent bioimaging of microalgal photophysiology and oxidative stress. **Photosynthesis Research**, v. 155, n. 2, p. 177-190, 2023. Doi: 10.1007/s11120-022-00989-6.

[84] Gerken, Lukas R. H. et al. Catalytic activity imperative for nanoparticle dose enhancement in photon and proton therapy. **Nature communications**, v. 13, n. 1, p. 1-14, jun. 2022. Doi: 10.1038/s41467-022-30982-5.

[85] Kessler, Amanda et al. Adsorption of Horseradish Peroxidase on Metallic Nanoparticles: Effects on Reactive Oxygen Species Detection Using 2′,7′-Dichlorofluorescin Diacetate. **Chemical Research in Toxicology**, v. 34, n. 6, p. 1481-1495, 2021. DOI: 10.1021/acs.chemrestox.0c00430.

[86] Zhao, Jiayuan; Riediker, Michael. Detecting the oxidative reactivity of nanoparticles: a new protocol for reducing artifacts. **Journal of nanoparticle research: an interdisciplinary forum for nanoscale science and technology**, vol. 16, n. 7, p. 1-13, 2014. Doi: 10.1007/s11051-014-2493-0.

[87] Boyles, Matthew et al. Development of a standard operating procedure for the DCFH2-DA acellular assessment of reactive oxygen species produced by nanomaterials. **Toxicology mechanisms and methods**, v. 32, n. 6, p. 439-452, jul. 2022. Doi: 10.1080/15376516.2022.2029656.

[88] Danaei, M. et al. Impact of particle size and polydispersity index on the clinical applications of lipidic nanocarrier systems. **Pharmaceutics**, v. 10, n. 2, p. 57, 2018. Doi: 10.3390/pharmaceutics10020057.

[89] Yeap, Swee Pin et al. Role of particle–particle interaction towards effective interpretation of Z-average and particle size distributions from dynamic light scattering (DLS) analysis. **Journal of Nanoscience and Nanotechnology**, v. 18, n. 10, p. 6957-6964, 2018. Doi: 10.1166/jnn.2018.15458.

[90] Maguire, Ciarán Manus et al. Characterization of particles in solution–a perspective on light scattering and comparative technologies. **Science and Technology of Advanced Materials**, v. 19, n. 1, p. 732-745, 2018. Doi: 10.1080/14686996.2018.1517587.

[91] Zheng, Tianyu; Bott, Steven; Huo, Qun. Techniques for accurate sizing of gold nanoparticles using dynamic light scattering with particular application to chemical and biological sensing based on aggregate formation. **ACS applied materials & interfaces**, v. 8, n. 33, p. 21585-21594, 2016. Doi: 10.1021/acsami.6b06903.

[92] Tang, Junqi et al. Hydroxide assisted synthesis of monodisperse and biocompatible gold nanoparticles with dextran. **Materials Science and Engineering: C**, v. 93, p. 759-767, 2018. Doi: 10.1016/j.msec.2018.08.045.

[93] Oliveira, Elisa et al. Synthesis and nuclear magnetic relaxation properties of composite iron oxide nanoparticles. **Química Nova**, v. 42, p. 57-64, 2019. Doi: 10.21577/0100-4042.20170309.

[94] Botteon, C. E. A. et al. Biosynthesis and characterization of gold nanoparticles using Brazilian red propolis and evaluation of its antimicrobial and anticancer activities. **Scientific Reports**, v. 11, n. 1, p. 1974, 2021. Doi: 10.1038/s41598-021-81281-w.

[95] Amendola, V. et al. Surface plasmon resonance in gold nanoparticles: a review. **J. Phys.: Condens. Matter**, v. 29, p. 1-48, 2017. Doi: 10.1088/1361-648X/aa60f3.

[96] Amendola, Vincenzo; Meneghetti, Moreno. Size evaluation of gold nanoparticles by UV− vis spectroscopy. **The Journal of Physical Chemistry C**, v. 113, n. 11, p. 4277-4285, 2009. Doi: 10.1021/jp8082425.

[97] Liu, Tianchi et al. Adhesive Gold Nanoparticles for Easy and Controlled Surface Coating. **Langmuir**, v. 35, n. 7, p. 2728-2737, 2019. Doi: 10.1021/acs.langmuir.8b04110.

[98] Fathy, Mohamed M. et al. An insight into synthesis and antitumor activity of citrate and gallate stabilizing gold nanospheres. **Scientific Reports**, v. 13, n. 1, p. 2749, 2023. Doi: 10.1038/s41598-023-29821-4.

[99] Yang, Song et al. Au-Pt Nanoparticle Formulation as a Radiosensitizer for Radiotherapy with Dual Effects. **International journal of nanomedicine**, v. 16, p. 239-248, jan. 2021. Doi:10.2147/IJN.S287523.

[100] Mazumdar, Samrat; Chitkara, Deepak; Mittal, Anupama. Exploration and insights into the cellular internalization and intracellular fate of amphiphilic polymeric nanocarriers. **Acta Pharmaceutica Sinica B**, v. 11, n. 4, p. 903-924, 2021. Doi:10.1016/j.apsb.2021.02.019.

[101] Okoampah, Emmanuel et al. Gold nanoparticles–biomembrane interactions: From fundamental to simulation. **Colloids and Surfaces B: Biointerfaces**, v. 196, p. 111312, 2020. Doi: 10.1016/j.colsurfb.2020.111312.

[102] Augustine, Robin et al. Cellular uptake and retention of nanoparticles: Insights on particle properties and interaction with cellular components. **Materials Today Communications**, v. 25, p. 101692, 2020. Doi: 10.1016/j.mtcomm.2020.101692.

[103] Yue, Jun et al. Gold nanoparticle size and shape effects on cellular uptake and intracellular distribution of siRNA nanoconstructs. **Bioconjugate chemistry**, v. 28, n. 6, p. 1791-1800, 2017. Doi: 10.1021/acs.bioconjchem.7b00252.

[104] White, Bryan E. et al. Cellular Uptake of Gold Nanorods in Breast Cancer Cell Lines. **Nanomaterials**, v. 12, n. 6, p. 937, 2022. Doi: 10.3390/nano12060937.

[105] Tsai, Shiao-Wen et al. Gold Nanoparticles Enhancing Generation of ROS for Cs-137 Radiotherapy. **Nanoscale Research Letters**, v. 17, n. 1, p. 123, 2022. Doi: 10.1186/s11671-022-03761-w.

[106] Kawamura, Kasumi; Qi, Fei; Kobayashi, Junya. Potential relationship between the biological effects of low-dose irradiation and mitochondrial ROS production. **Journal of radiation research**, v. 59, n. suppl_2, p. ii91-ii97, 2018. Doi: 10.1093/jrr/rrx091.

[107] Liu, Xi et al. The synergistic radiosensitizing effect of tirapazamine-conjugated gold nanoparticles on human hepatoma HepG2 cells under X-ray irradiation. **International Journal of Nanomedicine**, v. 11, p. 3517, 2016. Doi: 10.2147/IJN.S105348.

Pontifícia Universidade Católica do Rio Grande do Sul
Pró-Reitoria de Pesquisa e Pós-Graduação
Av. Ipiranga, 6681 – Prédio 1 – Térreo
Porto Alegre – RS – Brasil
Fone: (51) 3320-3513
E-mail: propesq@pucrs.br
Site: www.pucrs.br